



# Investigation of Capacitively Coupled Radio-Frequency Argon Plasma: Integration of in Situ Optical Diagnostics with Data-Driven and Theoretical Modeling

Sharona Atlas<sup>1,2</sup> · Shani Har Lavan<sup>1</sup> · Amir Kaplan<sup>2</sup> · Avi Lehrer<sup>1</sup> · Illya Rozenberg<sup>1</sup> · Hao Zhao<sup>3</sup> · Joshua H. Baraban<sup>1</sup>

Received: 3 November 2024 / Accepted: 30 March 2025 / Published online: 12 April 2025  
© The Author(s) 2025

## Abstract

We utilized a combination of experimental alongside data-driven and theoretical modeling techniques to study non-thermal plasma properties and observables including optical emission spectral intensities, electron temperature, species concentrations, degree of ionization, and reaction rates. As a case study we measured the plasma properties of Argon gas in the low-pressure regime using optical emission spectroscopy (OES) while varying plasma input power and gas flow rate. We used data-driven and drift-diffusion modeling techniques to obtain complementary information, including electron temperature, reduced electric field, and species densities. The calculated density number of excited argon has a linear correlation to measured emission intensity, and we found that the dominant effect on Ar I intensity is the applied power with the gas flow (or pressure) the secondary factor (77% and 20%, respectively). The electron temperature increases with power but decreases with flow (or pressure). Combining the measured and modelling results help to understand the cold plasma dynamics and chemistry towards more complex plasma chemistry applications.

**Keywords** Low-pressure plasma · Optical emission spectroscopy · Capacitively coupled plasma · Multivariate analysis · Drift-diffusion model

---

✉ Joshua H. Baraban  
jbaraban@bgu.ac.il

<sup>1</sup> Department of Chemistry, Ben-Gurion University of the Negev, P.O. Box 653, Beer-Sheva 84105, Israel

<sup>2</sup> Department of Chemical Engineering, Nuclear Research Center Negev, P.O. Box 9001, Beer-Sheva 84190, Israel

<sup>3</sup> College of Engineering, Peking University, Beijing 100871, PR China

## Introduction

Non-thermal plasmas (NTP) have garnered significant interest in recent years due to their ability to drive chemical reactions at low gas temperatures, thanks to highly energetic electrons compared to heavier ions and neutral atoms [1]. This provides benefits such as lower energy input, reduced toxicity, higher efficiency, and greater selectivity, making NTPs ideal for material synthesis, environmental cleanup, and biomedical applications [2–8]. NTPs are also being explored for waste treatment, with current applications including emission control of industrial compounds like soot, ammonia, and NO<sub>x</sub> [9]. Over the past two decades, atmospheric NTPs have been studied for air pollution control [10–13], enhanced combustion [6, 10, 11, 14], water and hydrocarbon dissociation [15–17] and the development of kinetic models for discharges of a variety of gases [18–23].

Low-pressure plasma (LPP), a subset of non-thermal plasma (NTP) operating below atmospheric pressure, offers unique advantages, including the highest electron temperatures among NTP types [24, 25]. LPP is widely used for material processing, particularly in modifying polymeric surfaces, etching silicon and silicon dioxide, and sterilizing medical instruments [26]. However, while extensively studied for material processing, its potential for waste treatment remains underexplored - a gap this study aims to address through combined experimental and modeling approaches.

To understand these systems, chemical studies of plasmas commonly employ *in situ* diagnostics to monitor their physical properties and chemical dynamics. Optical emission spectroscopy (OES) is one of the most powerful, well-established, and non-invasive diagnostic methods for characterization of plasmas [27]. However, the OES spectrum may not always give direct information on species densities and temperatures. Therefore, additional analysis of modeling excitation mechanisms and reaction kinetics in the plasma is often needed in order to calculate temperatures and concentrations and to provide valuable understanding of the fundamental chemistry in the plasma [28].

Plasma kinetics models can be classified into three main categories: kinetic, fluid, and hybrid. All methods essentially involve solving an appropriate transport equation along with Maxwell's equations. The first type, kinetic models, employ particle-tracking approaches [29–32]. These methods track the trajectories of individual charged particles in space and time, offer fine spatial resolution and are effective for modeling processes dominated by stochastic events, such as chemical reactions in plasmas and sputtering. However, they are computationally intensive, requiring significant resources for large systems [29, 33]. The most widely employed methods to describe the kinetic plasma dynamics are particle-In-cell Monte Carlo (PIC) and direct simulation Monte Carlo (DSMC) [30–37]. These kinetic models incorporate detailed descriptions of collision processes to account for interactions between particles, which are essential for accurately modeling energy transfer, particle creation and loss, and the evolution of velocity and energy distributions in the plasma. Collisional-Radiative Models (CRM), often considered a specialized subset of kinetic models, involve solving a set of coupled rate equations that describe the populations of different energy levels due to collisional and radiative processes [38–40]. CRMs are essential tools in plasma physics for analyzing atomic and molecular processes, particularly in low-temperature plasmas. These models determine the distribution functions of excited states as functions of plasma parameters such as electron temperature, electron density, and ground-state densities. By accounting for processes like spontaneous transitions, electron impact

excitation and ionization, recombination, photon-induced transitions, and atom-induced collisions, CRMs provide a comprehensive framework for understanding the population and depopulation dynamics of excited, vibronic, and ionized states [38–40]. Similarly to PIC method, the CRM is a powerful tool providing a detailed and accurate description of the plasma species but at the cost of complexity and computational resources. Many of the kinetic model studies that exist present the aspects of chemical deposition and thin film applications [41–48]. The second category is fluid, or continuum, models. These models are based on a theoretical hydrodynamic description of the plasma [49]. This approach simplifies the complex interactions of plasma particles by treating the plasma as a continuous medium rather than a collection of individual particles. Many of the fluid models use the drift-diffusion approximation to describe the collective behavior of charged particles under electromagnetic forces and interactions [50–56]. The numerical solution of fluid models is computationally efficient and can model large-scale plasma systems. Therefore, this approach provides an attractive alternative for practical applications, such as analysis of CCRF discharges [51]. The third computational category is hybrid, combining particle-based and fluid-based methods to simulate plasmas. It aims to leverage the strengths of both techniques while mitigating their individual limitations. The most common hybrid model, the Fluid-EEDF hybrid, combines a fluid description of the discharge with electron transport properties and reaction rate coefficients derived from the electron energy distribution function (EEDF). The EEDF is determined by solving the Boltzmann equation, either directly or using a Monte Carlo approach. The fluid module includes equations for species mass, momentum, and energy continuity, as well as Poisson's equation for the electric field, but does not require an equation for mean electron energy, as the EEDF is part of the solution [35, 49, 57–61]. Further information about kinetic, fluid and hybrid plasma models, including their applications and limitations, can be found in reference [62]. The choice of the modeling method depends on the specific plasma system, the level of detail required, and the computational resources available.

The three categories of models described above are purely theory based. While these three traditional categories of models provide valuable insights, they face significant limitations, including the complexity of plasma kinetics, large uncertainties in predictions, limited availability of measurement data, and high computational costs. These challenges underscore the need for alternative approaches to overcome these obstacles. Thus, it is noteworthy that in the past few years, a new empirical type of modeling approach, has been gaining momentum [63–66]. These data-driven methods are primarily based on observational data to make predictions or understand patterns, without necessarily being bound by pre-established theories, making them particularly useful in systems where relationships between variables are complex and not fully understood yet through tractable theoretical models. These models utilize statistical, computational, and machine learning techniques to calculate outcomes and derive insights. For example, Takagi et al. proposed a statistical approach using multivariate scaling to predict the maximum proton energy through target normal sheath acceleration. They derived scaling laws for the experimental parameters, the hot electron temperature and density observed in the corresponding PIC simulations. They demonstrated the effectiveness of this approach in predicting the maximum proton energy and provide the experimental conditions required to achieve a proton energy exceeding 100 MeV [67]. Djordjevic et al. employed a neural-network-based approach, adapting an ensemble of over 1000 one-dimensional (1D) PIC simulation data to train the network. Based

on that, they developed a predictive model capable of rapidly forecasting proton energy under different plasma conditions, enabling feature discovery that would not be feasible with traditional parameter scans due to their high computational cost [68]. In the plasma field, these models have become increasingly important and thus they are implemented in diagnostics and monitoring, process control and optimization, system design and predictive maintenance [63–66, 69–74]. A recent perspective highlights the transformative role of data-driven methods in plasma science, emphasizing how these approaches leverage large datasets produced by experiments and simulations in plasma research [71]. The authors claim that data-driven methods will be crucial for reshaping exploration, understanding and optimizing plasma systems that have been hitherto very difficult to analyze theoretically due to nonlinearities and complexity present in these systems. Another comprehensive review outlines significant advancements in the interdisciplinary field of data-driven plasma science. The authors emphasize how data-driven approaches are revolutionizing plasma science by leveraging massive datasets generated from experiments, observations, and simulations to achieve improvements in diagnostics, process control, optimizing plasma conditions, as well as enhancing efficiency and outcomes [75].

In this study, we implemented two distinct types of models: a data-driven model and a drift-diffusion fluid model. This combined approach leverages the strengths of both methods: the data-driven model utilizes advanced statistical techniques to interpret the data and predict patterns, while the drift-diffusion fluid model offers a more traditional, physics-based approach to understanding the plasma dynamics. Together, they provide a comprehensive and effective modeling solution to complement our experimental approach.

Modeling plasma kinetics is a challenging task, and low-pressure systems are even more difficult to model, since they are not in thermodynamic equilibrium. One example is a study by Marques et al. where they developed a kinetic model for hydrogen discharge in a capacitively coupled radio frequency (CCRF) plasma, with pressure between 0.2 and 1 Torr, including vibrationally excited molecular species and electronically excited atomic species [76]. If the system is fed by a mixture of gases, such as air or water with carrier gas, the complexity involved to model and predict desired plasma properties and/or products grows exponentially, due to the proliferation of simultaneous reactions. In such a case some assumptions are needed, such as simplifying geometry (reducing the model dimensionality) and focusing on only a handful of species.

Therefore, our strategy for exploring LPP for waste treatment begins with characterizing our experimental system and modeling capabilities using Argon, before moving towards more complex cases such as hydrocarbons. Pure Argon has a manageable and well-known set of plasma reactions (as described later in this paper). Additionally, Argon plasma is extensively characterized in the literature through spectroscopic methods [77–83], and modeling studies [84–93]. In this paper, we investigate and model low-pressure Argon plasma to establish a foundation for optimizing the plasma system for hydrocarbon decomposition. We present and demonstrate a methodology for predicting plasma properties, focusing on chemical aspects, using experimental data, theoretical calculations, and multivariate quantitative analysis of the measured data. A key part of this approach involves developing a protocol to connect and correlate *in situ* OES measurements with species densities and temperatures. While calculations of densities and temperatures provide microscopic insights into experimental data, they are computationally intensive. The integration of OES measurements with these calculations is complementary and enhances understanding. This joint

experimental and computational framework lays the groundwork for future studies involving more complex chemistries, such as those required for environmental applications and a graded two-step waste treatment process involving pyrolysis followed by decomposition of pyrolysis product gases using LPP.

## Methods

Our research tools include a plasma reactor for in situ OES measurements, a data analysis protocol interfaced with an empirical multivariate model for calculation of plasma properties under different conditions, and theoretical simulations of the plasma.

## Experimental Setup

A schematic of the various aspects of our experimental setup (gas handling, plasma reactor, and analysis) is shown in Fig. 1. Gas flow is controlled by a set of mass flow controllers (MFCs). The typical flow in our system is between 5 and 100 sccm to maintain LPP conditions (10–1000 mTorr) using a dry Roots pump (Kashiyama NeoDry 36 E). Generally, the pressure is used to describe plasma systems, since it determines the species densities and their collision rates, which directly affect the plasma properties and reactions; they also influence the plasma ignition, sustainment, and confinement. However, in our system, the controlled variable is the flow rate, while the pressure is a consequence of the flow and feed composition, as well as the reactor geometry and pump. In this study, experiments were conducted within an applied power range of 10–300 W and a gas flow rate range of 10–100 sccm. The pressure range corresponding to this range of gas flow is 75–376 mTorr, and the correlation between them is linear. Applied power is controlled between 20 and 300 W; the voltage range calculated according to the applied power is 300–1800 V. Detailed experiments matrix, and the working conditions is provided in Table SI-1. The plasma chamber, shown in Fig. 1(b), generates capacitively coupled plasma (CCP) by a 13.56 MHz radio-frequency generator between RF and ground electrodes. The plasma gap is 10 cm, and each electrode has a diameter of 26 cm. The optical emission spectroscopy (OES) capabilities are based on a medium resolution spectrograph (Ocean Optics, FLAME-S-XR1-ES, wavelength range: 200–1025 nm, optical resolution: 0.5 nm FWHM).

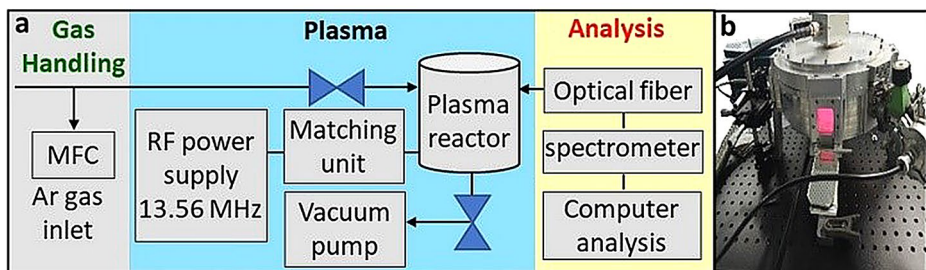


**Fig. 1** Experimental setup: (a) general scheme of the low-pressure plasma system; (b): plasma reactor with Ar discharge glow

## Modeling

### General Strategy

The complexities of non-equilibrium cold plasma systems (for example, non-uniform temperature and electron density distribution) make model-aided analysis highly advantageous. To complement the information received from the OES diagnostics, two types of modeling (empirical data-driven and theoretical fluid drift diffusion) were conducted in parallel with the experiments. With these models we can predict the optical emission as a function of plasma conditions and provide additional information such as temperature and species concentration variations, for validation against experimental results. Our modelling strategy is described in Fig. 2.

### Empirical Data-Driven Model

The influence of plasma power and pressure on the emission intensities in Argon plasmas has been reported in the literature and our results are consistent with existing knowledge (as will be shown in Sect. 3.2) [28, 81]. These published studies examine each of these factors individually and provide separate information on the influence of plasma power and pressure on emission intensities. To further analyze the relationship between the emission intensities (response function) and the independent variables (plasma power and pressure/flow), we performed a multivariate analysis to develop a comprehensive model that incorporates both parameters simultaneously, while accounting for their combined influence.

Multivariate analysis is a powerful statistical approach used to examine relationships between multiple variables at once, considering their interdependencies and potential interactions. This methodology enables the creation of models that go beyond simple one-variable-at-a-time analysis, allowing for a deeper understanding of complex systems where multiple factors contribute to the observed outcomes.

The empirical model is based on a statistical multivariate technique that captures the combined effects of plasma power and gas flow rate (or pressure) on the emission intensities, taking into account their interdependencies and interactions. By applying this method to our database of results, we can predict observations for unmeasured sets of conditions, and extract insights into how variations in gas flow rate and applied power affect the measured emission intensities. It should be noted that OES measurements are often used to develop predictive data-driven models that are designed to estimate and control plasma reactor performance. This concept is often referred to as virtual metrology, and it is particularly prevalent in semiconductor manufacturing where direct measurement of process outcomes can be costly or technically challenging [75].

The quantitative analysis software JMP-SAS was used to describe and predict the intensities of selected Ar emission line signals as functions of working conditions [94], ultimately constituting the model “A”. We explored a variety of models and methods to determine the most suitable functional form that describes the relationship between the intensity as a dependent variable and the controlled variables, power and flow. The criteria for choosing the final model equation are the quality of the fit, and equally if not more important, the ability to explain the plasma physics with this model form.

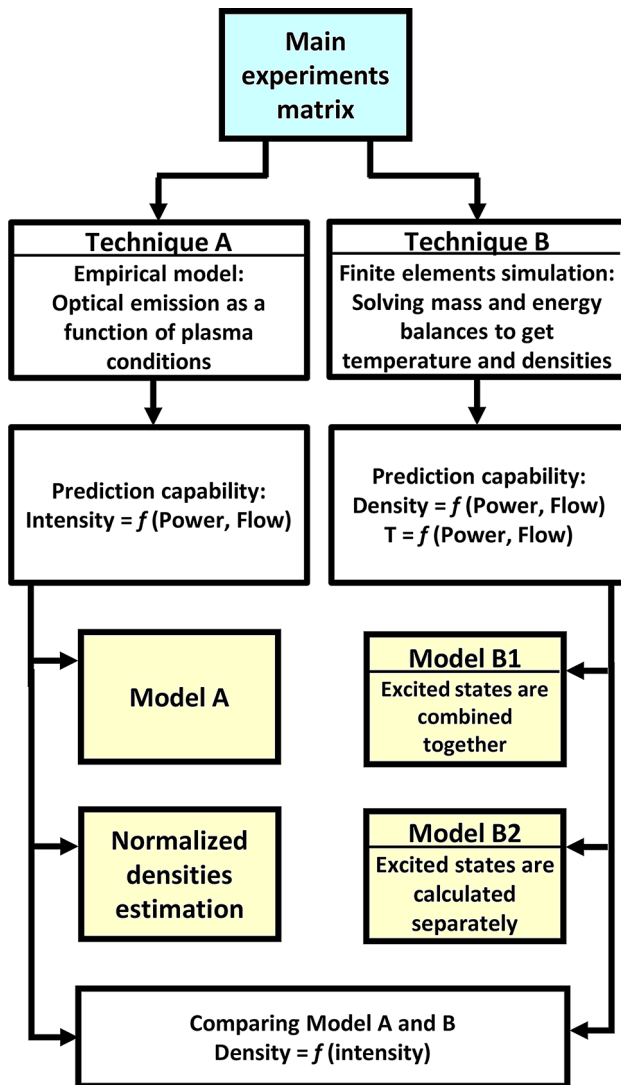


Fig. 2 Modeling strategy

### Theoretical Modeling Using Drift-Diffusion Fluid Model

**General Description** Plasma models are well-known to be computationally intensive, especially for a CCP system [29]. Here we constructed a simplified drift-diffusion model for our CCP reactor, using a finite element method by implementing the plasma module of COMSOL Multiphysics ver. 6.1 [95]. The COMSOL modeling workflow includes the following main steps: defining geometry, specifying material properties, defining the physics and its boundary conditions, creating the computational mesh, defining the plasma chemistry, running simulations, and post-processing the results. The resulting model will be referred to

as model “B”. This subsection will describe the details of model B according to the above workflow.

Due to the complex challenges of plasma modelling, we have constructed our model in a one-dimensional (1D) geometry. The dimension solved in the model is the plasma gap, i.e., the distance between the two electrodes, which is 10 cm. On one side of the gap a sinusoidal RF power is applied, and the other side is electrically grounded; the circuit impedance is matched, as in the experiments. This geometry represents our chamber dimensions and is shown in Fig. 3. The model was run for pressure range of 75–376 mTorr, which corresponds to our working flow range of 10–100 sccm.

After defining the physics in the model, the next significant step is constructing the modeling mesh. The mesh is divided into 450 computational elements, where the size of each element decreases proportionally with its distance from the center. The smallest elements are adjacent to the electrodes and the largest element is in the center of the plasma, such that the sheath regions have a finer mesh than the bulk region. This type of mesh is appropriate to the plasma physics and efficient computationally. Further details regarding the mesh elements’ sizes are shown in Figure SI-1.

We used the plasma-time-periodic numerical method for modeling our CCP reactor. In such systems, an overwhelming number of RF cycles is required before the plasma evolves to a time-periodic steady-state solution. Instead of solving in the time domain, the time is introduced as an extra dimension to the underlying mathematical equations. This extra dimensional equation represents one RF cycle and enforces periodic boundary conditions. This avoids having to solve thousands of RF cycles and dramatically reduces computation time [95]. The Time periodic study is basically equivalent to the steady-state solution. We have also used the time-dependent study function of the plasma module, which allows us to simulate the plasma from ignition to steady-state.

In general, for higher fidelity in drift-diffusion models, the Debye length should be small relative to the system’s characteristic length scale ( $\lambda_D < d$ ) [53]. The Debye length represents the scale at which plasma achieves neutrality; thus, smaller Debye lengths can correspond to higher ionization levels, leading to more accurate plasma behavior modeling. Here, the Debye length is about 2.5 cm while  $d$  is 10 cm. According to [96], the pressure limit for validity of such a model in a typical CCP reactor with  $d = 3\text{--}10$  cm is about 10 mTorr, which is compatible with the pressure range used in our experiments. Furthermore, we implemented the Druyvesteyn EEDF in our drift-diffusion model, which should be more appropriate than the Maxwellian EEDF for this pressure range [55]. Additionally, the spatial resolution of the model must be fine enough to adequately resolve the Debye length. Accordingly, the model

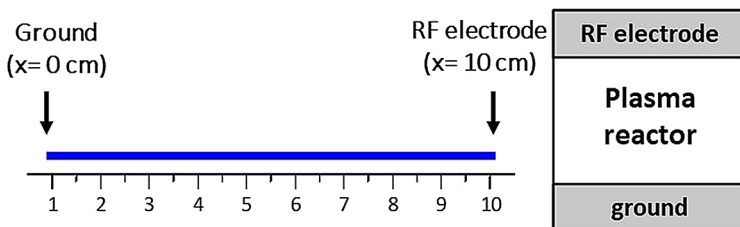


**Fig. 3** Model geometry

mesh has been carefully designed so that the sheath zones are significantly finer than the bulk zone (as shown in Figure SI-1).

Although drift-diffusion plasma fluid models are computationally efficient, they have certain limitations that must be carefully considered, especially at low pressures. One key challenge is that charged species are strongly coupled to the electric field, which imposes strict constraints on the time step when using an explicit time integrator. High plasma conductivity can further restrict the time step, making the simulation more computationally demanding. Additionally, in regions with sharp density and electric field gradients, electrons may unphysically diffuse parallel to the field, leading to unrealistic ionization [97]. For example, Datta et al. conducted 1D drift-diffusion simulations of argon CCPs in the pressure range of 10–150 mTorr using COMSOL. Their results of electron density, electron temperature and plasma potential have shown good agreement with experiments for the pressure above 60 mTorr, while at low pressure, it seems that the simulations and the experiments do not match for plasma potential [98]. Yang et al. applied a 2D drift-diffusion model for ICPs with pressures between 100 and 1000 mTorr. Their calculated values of electron temperature and electron density exhibit good agreement with the trend in their experiment results [99]. Brezmes et al. reported accurate modeling at 1.33 Pa (approximately 10 mTorr) of RF ICP, based on a new approach. They used the COMSOL Magnetic Field interface to calculate the input inductive power, followed by a CCP interface calculation of species transport and the capacitive power coupled to the system [100]. Jia et al. implemented a drift-diffusion model for ICP at 10 mTorr using COMSOL. The authors attribute the difference between calculated and measured electron energies to the existence of a high energy tail of the Maxwellian electron energy distribution function (EEDF), while the calculated and experimental distribution profiles exhibit a similar overall shape [55]. Gao et al. measured electron density and temperature, showing trends that aligned well with COMSOL simulations at 2 Pa across for different powers in a RF ICP system. They found that the calculated electron temperature was consistently higher, while electron density was underestimated at 2 kW, with better agreement at lower RF power. The discrepancy was attributed to the reduced chemistry set in the simulation and inefficient power coupling at high RF power and pressure below 1 Pa [101]. Further discussion on the limitations of drift-diffusion models and various approaches to mitigate these challenges to their accuracy can be found in [102–110].

**Governing Equations** Drift diffusion equations are used to calculate the transport of electrons and electrons energy.

The equation that governs the electron density is:

$$\frac{\partial n_e}{\partial t} + \nabla \cdot \Gamma_e = R_e - \mathbf{u} \cdot \nabla n_e \tag{1}$$

Definition of the electron flux vector:

$$\Gamma_e = -(\mu_e \cdot \mathbf{E}) n_e - D_e \cdot \nabla n_e \tag{2}$$

Where  $n_e$  is the electron density ( $1/\text{m}^3$ ),  $\Gamma_e$  is the electron flux vector, ( $1/(\text{m}^2\text{s})$ ),  $R_e$  is electron rate expression, ( $1/(\text{m}^3\text{s})$ ),  $\mathbf{u}$  is the neutral fluid velocity vector ( $\text{m/s}$ ),  $\mu_e$  is the electron mobility ( $\text{m}^2/(\text{V}\cdot\text{s})$ ),  $\mathbf{E}$  is the electric field ( $\text{V/m}$ ), and  $D_e$  is the electron diffusivity ( $\text{m}^2/\text{s}$ ).

Rate of change of the electron energy density is given by (the subscript  $\epsilon$  refers to electron energy):

$$\frac{\partial n_\epsilon}{\partial t} + \nabla \cdot \Gamma_\epsilon + \mathbf{E} \cdot \Gamma_\epsilon = S_{en} - (\mathbf{u} \cdot \nabla) n_\epsilon + (Q + Q_{gen})/q \quad (3)$$

Definition of the electron energy flux:

$$\Gamma_\epsilon = -(\mu_\epsilon \cdot \mathbf{E}) n_\epsilon - D_\epsilon \cdot \nabla n_\epsilon \quad (4)$$

Where  $n_\epsilon$  is the electron energy density ( $\text{V/m}^3$ ),  $\Gamma_\epsilon$  is the flux of electrons energy vector, ( $\text{V}/(\text{m}^2\text{s})$ ),  $S_{en}$  is the energy loss/gain due to inelastic collisions ( $\text{V}/(\text{m}^3\cdot\text{s})$ ),  $Q$  is external heat sources ( $\text{W/m}^3$ ),  $Q_{gen}$  is a generalized heat source ( $\text{W/m}^3$ ),  $q$  is the electron charge (C),  $\mu_\epsilon$  is the electron energy mobility ( $\text{m}^2/(\text{V}\cdot\text{s})$ ), and  $D_\epsilon$  is the electron energy diffusivity ( $\text{m}^2/\text{s}$ ).

The heavy species, which include neutrals, ions and excited state of argon, are calculated as follows.

Assuming a reacting flow consists of  $k=1, \dots, Q$  species and  $j=1, \dots, N$  reactions, the equation for the first  $Q-1$  species is given by:

$$\rho \frac{\partial}{\partial t} (\omega_k) + \rho (\mathbf{u} \cdot \nabla) \omega_k = \nabla \cdot \mathbf{j}_k + R_k \quad (5)$$

$$\sum \omega_i = 1 \quad (6)$$

Where  $\mathbf{j}_k$  is the diffusive flux vector,  $\omega_k$  is the mass fraction of the  $k^{\text{th}}$  species,  $\rho$  is the density of the mixture ( $\text{kg}/\text{m}^3$ ),  $R_k$  is the rate expression for species  $k$ ,  $\text{kg}/(\text{m}^3\cdot\text{s})$ .

The diffusive flux vector is defined as:

$$\mathbf{j}_k = \rho \omega_k \mathbf{V}_k \quad (7)$$

Where:

$\mathbf{V}_k$  is the multicomponent diffusion velocity for species  $k$ .

Detailed descriptions of heavy species transport can be found in Plasma Module User's Guide version 6.2 COMSOL Multiphysics [95].

**The Wall Boundary Conditions** Boundary conditions in plasma modeling play a critical role in determining the interactions between the plasma species and its surrounding environment, particularly at the walls. At the wall, several mechanisms govern the exchange of electrons: (a) Loss of electrons due to a net flux of electrons from the plasma bulk to the wall; (b) loss of electrons due to the random motion of electrons within the mean free path of the wall; (c) gain of electrons due to secondary emission; a wall emits an electron with some

probability when it is struck by an ion or other excited species; and (d) Gain of electrons due to thermionic emission.

General wall setting in the model:

- The flux of electrons lost to the wall is self-consistently computed based on the electron temperature and electron density adjacent to the wall.
- Mean thermionic energy is set to zero (no electrons are being emitted from the wall due to thermionic emission).
- Surface reactions set up the reactions involving gas phase species on surfaces. This typically involves first-order reactions on surfaces where excited or ionic species transition back to their ground state. The reaction parameters are forward sticking coefficient ( $\gamma_f$ ), secondary emission coefficient ( $\gamma_i$ ), and mean energy of secondary electron ( $\epsilon_i$ ). For excited states  $\gamma_f$  is set to 1 and for ions to zero.  $\gamma_i$  is set to 0.07 for all species and  $\epsilon_i$  is set to 5.8 eV for all species. The flux due to secondary emission is computed automatically based on the defined surface reactions.

**Reactions Set** Modeling the plasma chemistry requires choosing a set of electron impact and species collision reactions that result in ionization, excitation, and attachment. These data sets are extensively discussed in [111–116].

Model B has two sub-variations, B1 and B2. Model B1 is a simplified model, in which all the electronic levels of excited Ar are considered as only a single species. The rate coefficients for this model were calculated from cross-sections imported from the LXCat database [117, 118]. The dataset includes the following species: ground state Ar, excited Ar, ionized Ar, and the electron. The process that produces doubly ionized Ar is taken from [88]. For excited Ar, the model is simplified by representing the first four 1s levels of excited argon (Paschen labels 1s2 to 1s5) as a combined level, and the next ten levels (2p1 to 2p10) are not included at all.

Model B2 distinguishes between different excited states, according to the approach suggested in [120]: the two metastable states are grouped together and called Ar<sup>m</sup>, two resonant states are grouped together and called Ar<sup>r</sup> and, the ten 4p levels are defined as state Ar<sup>p</sup>. The reactions that are included in model B1 and B2 are presented in Tables 1 and 2 accordingly.

As will be shown below, in the end we compared intensity data and results from model A with calculated densities from models B1/B2 to quantify species densities in the plasma, and to get a direct correlation between measured intensities and species densities.

## Results and Discussion

### Spectrum Identification

Significant information about the plasma dynamics can be extracted from OES spectra, including plasma stability, identifying various species within the plasma and insights into the densities of these species.

**Table 1** Elementary processes included in the simplified model B1 and the corresponding references for the cross sections or forward rate constants

#	Process	Notation	<sup>(a)</sup> k <sup>f</sup>	Ref.
R1	Elastic scattering	$e^- + \text{Ar} \rightarrow e^- + \text{Ar}$	(b)	[117]
R2	Excitation	$e^- + \text{Ar} \rightarrow e^- + \text{Ar}^*$	(b)	[117]
R3	De-excitation	$e^- + \text{Ar}^* \rightarrow e^- + \text{Ar}$	(b)	[117]
R4	Direct ionization	$e^- + \text{Ar} \rightarrow 2e^- + \text{Ar}^+$	(b)	[117]
R5	Stepwise ionization	$e^- + \text{Ar}^* \rightarrow 2e^- + \text{Ar}^+$	(b)	[117]
R6	Dissociative recombination	$e^- + \text{Ar}_2^+ \rightarrow \text{Ar} + \text{Ar}$	4.5e14	[88]
R7	Penning ionization	$\text{Ar}^* + \text{Ar}^* \rightarrow e^- + \text{Ar} + \text{Ar}^+$	7.2e8	[88]
R8	Radiation	$\text{Ar}^* \rightarrow \text{Ar} + h\nu$	1.66e8	[119]
R9	Molecular ion formation	$\text{Ar} + \text{Ar} + \text{Ar}^+ \rightarrow \text{Ar}_2^+ + \text{Ar}$	9.1e4	[88]
R10	Diffusion	$e^-, \text{Ar}^*, \text{Ar}^+, \text{Ar}_2^+ \rightarrow \text{wall}$	-	[88]

(a)  $k^f$  in  $\text{m}^3/(\text{s} \cdot \text{mol})$  for reactions number 1–7, 1/s for reaction number 8 and  $\text{m}^6/(\text{s} \cdot \text{mol}^2)$  for reaction number 9

(b) Forward rate constant is calculated according to cross section dataset

The first step is identification of the emission transitions and the excited states from which they originate. Figure 4 presents the measured emission spectrum of Ar with 50 W plasma power at a flow rate of 50 sccm (225 mTorr). The obtained Ar emission lines, lying typically between 700 and 850 nm, are in good agreement with the NIST Atomic Spectra database [119] and accordingly the related upper states are known. It should be noted that although only argon gas was introduced into the system, signatures of nitrogen are seen in the spectrum, due to unavoidable trace amounts of air. The supporting information shows additional OES spectra taken under various operational conditions (Figures SI-2 to SI-4).

## Observed Trends

The second step is monitoring the dependence of the transition intensities on the plasma conditions. Figures SI-5 presents intensities of specific peaks obtained from our experimental system, under different flow rates and applied power. This broad overview provides quantitative information about the impacts of plasma power and gas flow rate on the intensity of these peaks of interest.

As seen in the OES spectra, increasing the flow rate from 10 to 100 sccm (corresponding to 75–376 mTorr) under constant RF power results in increased intensity of the line at 764 nm, which corresponds to the  $3s^23p^5(2P^0_{3/2})4p^2[3/2] \rightarrow 3s^23p^5(2P^0_{3/2})4s^2[3/2]$  Ar I transition and signifies an increase in the upper state population with flow rate. A similar trend can also be seen in the spectra for the emission lines at 802 and 812 nm. In all three cases the intensities reach saturation at a certain flow rate but continue to increase with increasing RF power.

The observed correlations between emission intensity and species density are discussed further in Sect. 3.3.

## Multivariate Analysis of the Raw data– Model A

The third step is conducting a multivariate analysis to gain a better understanding of the relationship between the operational working conditions and the experimental OES results.

**Table 2** Processes included in the model B2

#	Process	<sup>(a)</sup> k <sup>f</sup>	Ref.
R1	$e^- + Ar \rightarrow e^- + Ar$	$f(\epsilon)$	[117]
R2	$e^- + Ar \rightarrow Ar^+ + e^- + e^-$	$f(\epsilon)$	[117]
R3	$e^- + Ar^m \rightarrow Ar^+ + 2e^-$	$2.99 * 10^{-13} T_e^{0.22} e^{-4.73/T_e}$	[120]
R4	$e^- + Ar^f \rightarrow Ar^+ + 2e^-$	$3.28 * 10^{-13} T_e^{0.21} e^{-4.51/T_e}$	[120]
R5	$e^- + Ar \rightarrow Ar^m + e^-$	$9.90 * 10^{-16} T_e^{-0.08} e^{-11.72/T_e}$	[120]
R6	$e^- + Ar \rightarrow Ar^+ + e^-$	$4.03 * 10^{-15} T_e^{0.45} e^{-12.12/T_e}$	[120]
R7	$e^- + Ar \rightarrow Ar(4p) + e^-$	$9.26 * 10^{-15} T_e^{-0.06} e^{-14.24/T_e}$	[120]
R8	$e^- + Ar(4p) \rightarrow Ar^+ + 2e^-$	$1.23 * 10^{-12} T_e^{0.25} e^{-3.71/T_e}$	[120]
R9	$e^- + Ar^m \rightarrow Ar(4p) + e^-$	$2.48 * 10^{-12} T_e^{-0.16} e^{-1.88/T_e}$	[120]
R10	$e^- + Ar^m \rightarrow Ar^+ + e^-$	$3.70 * 10^{-13}$	[120]
R11	$e^- + Ar^f \rightarrow Ar^m + e^-$	$9.10 * 10^{-13}$	[120]
R12	$e^- + Ar^f \rightarrow Ar(4p) + e^-$	$2.48 * 10^{-12} T_e^{-0.16} e^{-1.79/T_e}$	[120]
R13	$e^- + Ar^m \rightarrow Ar + e^-$	$2.25 * 10^{-16} T_e^{-0.17} e^{-1.65/T_e}$	[120]
R14	$e^- + Ar^f \rightarrow Ar + e^-$	$6.82 * 10^{-16} T_e^{0.44} e^{-0.43/T_e}$	[120]
R15	$e^- + Ar(4p) \rightarrow Ar + e^-$	$2.97 * 10^{-16} T_e^{-0.11} e^{-1.38/T_e}$	[120]
R16	$e^- + Ar(4p) \rightarrow Ar^m + e^-$	$4.16 * 10^{-13} T_e^{-0.17} e^{-0.32/T_e}$	[120]
R17	$e^- + Ar(4p) \rightarrow Ar^+ + e^-$	$4.16 * 10^{-13} T_e^{-0.17} e^{-0.32/T_e}$	[120]
R18	$Ar^m + Ar^m \rightarrow 2Ar$	$2.00 * 10^{-13}$	[120]
R19	$Ar^m + Ar^f \rightarrow Ar + Ar^+ + e^-$	$2.10 * 10^{-15}$	[120]
R20	$2Ar(4p) \rightarrow Ar + Ar^+ + e^-$	$5.00 * 10^{-16}$	[120]
R21	$2Ar^m \rightarrow Ar + Ar^+ + e^-$	$6.40 * 10^{-16}$	[120]
R22	$Ar + Ar^m \rightarrow 2Ar$	$2.10 * 10^{-21}$	[120]
R23	$Ar^f \rightarrow Ar + h\nu$	$1.00 * 10^5 S^{-1}$	[120]
R24	$Ar(4p) \rightarrow Ar + h\nu$	$3.20 * 10^7 S^{-1}$	[120]
R25	$Ar(4p) \rightarrow Ar^m + h\nu$	$3.00 * 10^7 S^{-1}$	[120]

The outcome of this analysis is Model A. The importance of model A is the ability to predict the emission intensities (and then the species densities, as will be explained in Sect. 3.4) as a function of the control variables— plasma power and gas flow rate. Alternatively, for any desirable intensity outcomes the combination of flow rate and plasma power can be easily found, as will be demonstrated below.

This section demonstrates the model results on one example of emission intensity at 752 nm. The functional form of the emission intensity depends on a complex interplay of various factors, including the specific excitation and radiative decay processes involved, the energy levels of the transitions and the plasma conditions. Based on the underlying plasma physics, the emission intensity ( $I$ ) can be described by the following general equation:

$$(1) I_{ij} = a * A_{ij} * k(T_e) * n_e * n_{gas}$$

Where:

$A_{ij}$  represents the transition rate from level  $i$  to  $j$

$k(T_e)$  is electron-impact excitation rate

$n_e$  is the electron density,

$n_{gas}$  is the gas density number,

and  $a$  is proportionality constant for a specific emission process.

Assuming the electron density exhibits a direct proportionality to the applied power, the gas density follows a similar trend with the flow rate, and the excitation rate is either inversely proportional to the flow rate (1/flow) or independent of flow, Eq. (1) simplifies, resulting in the following concise and practical expression:

$$(2) I_{ij} = a_k * (Power) * (Flow)^p$$

Where:

$a_k$  is a constant that includes the transition and excitation rates and  $p$  is the power fitting parameter that indicates the dependence of excitation rate on temperature.

The final model equation that emerged is:

$$(3) I = a_0 + a_1 (Power) + a_2 (Flow) + a_3 (Flow)^2 + a_{12} (Power) * (Flow)$$

where:

$I$  is the emission intensity at a specific wavelength,

$Power$  is the applied power in W,

$Flow$  is the gas flow in sccm,

and  $a_0, a_1, a_2, a_3$  and  $a_{12}$  are the model coefficients.

The formulated model equation comprises five terms: one is the constant term,  $a_0$ , and another four terms that describe the independent variables. The constant term represents the threshold behavior inherent to the system, and therefore, its inclusion within the model equation is practically essential even though the threshold behavior is outside the scope of our study. This is consistent with the observations and description in the literature that show that at zero power the extrapolated intensity line exhibits a notable deviation from zero intensity [28]. This phenomenon can be attributed to the presence of an ignition threshold, indicating that a minimal level of energy input is required to initiate the plasma ignition and the emission process. The other four coefficients in the equation represent the effects of each parameter on the emission intensity, taking into account the combined influence of both variables. The terms  $a_1 (Power)$  and  $a_{12} (Power) * (Flow)$  fit the structure of Eq. (1) with  $p=0,1$  but in addition to the gas density that is taken into account by the latter term, we have found that a  $p=2$  term is necessary due to the effect of the fluid dynamics, beyond that of the plasma discharge alone. The model A formula is therefore clearly consistent with

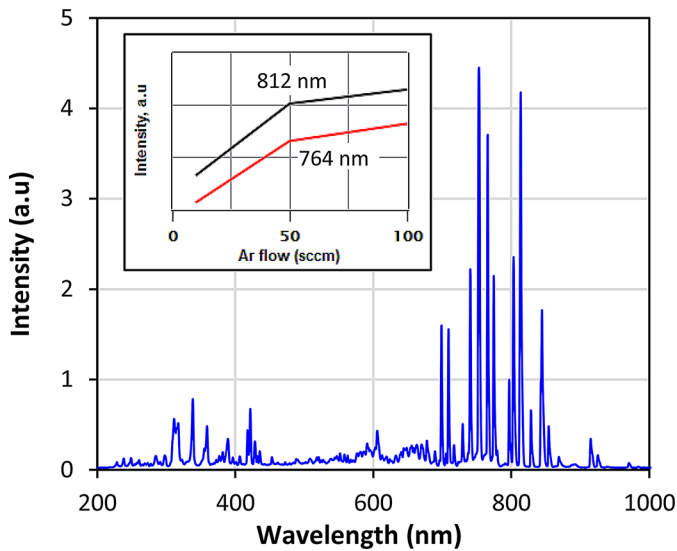


**Fig. 4** Ar emission spectrum measured at plasma power of 50 W, and gas flow of 50 sccm (225 mTorr). The inset displays the trends of two representative peaks over three different gas flow rates and the same plasma power

a physics-based understanding of and the physical constraints on the plasma system, even though it is a data-driven model derived solely by data science techniques.

Model A was built principally for transitions involving excited Ar I because this is the predominant species in the plasma. The model equation is similar for all the Ar I wavelengths that were modeled, and only the coefficients vary moderately. The model coefficients for each transition are presented in Table SI-2.

Model A was verified by additional experiments, where the measured intensity was compared with the predicted results, as presented in Table SI-3. Accordingly, this model can predict characteristic optical emission and the related Ar excited state density over a wide range of combinations of working conditions. It should be noted that given the power law nature of the model, extrapolation of the model should only be done warily. We tested the largest range possible according to our system limitations of flow and applied power, and therefore verification of the model could be performed only within this range.

By analyzing the model formula, we can break down the influence of the individual parameters on the response function, as shown in Fig. 5 (the overall analysis excluded the constant term, since its physical meaning is irrelevant here). This analysis is based on Pareto ANOVA method, which identify and rank the most influential factors affecting a response variable in a process or experiment. It is particularly useful in identifying significant factors in designed experiments or statistical regression models, like model A presented here. This method is commonly applied in context of process optimization or quality improvement to evaluate the relative significance of various factors or the effects of predictors in the statistical model. Further explanation about the method and its implementation can be found in references [121–123], and the relative significance of various factors of predictors in the statistical model A are shown in Figure SI-6. According to the Pareto analysis, it was found that the dominant effect on the intensity of the peak at 752 nm is the linear term in applied

**Fig. 5** Influence of parameters on the intensity of 752 nm emission

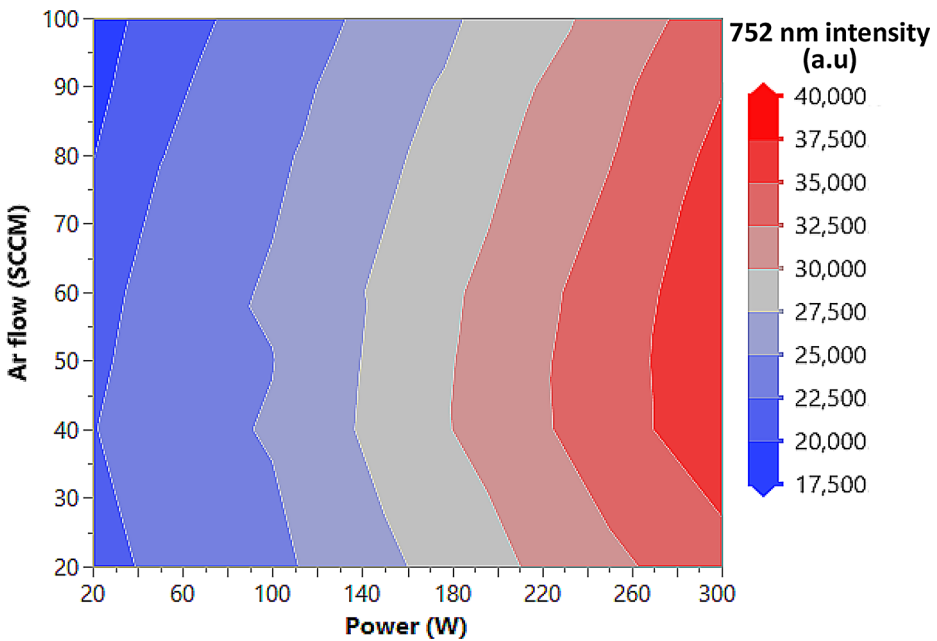
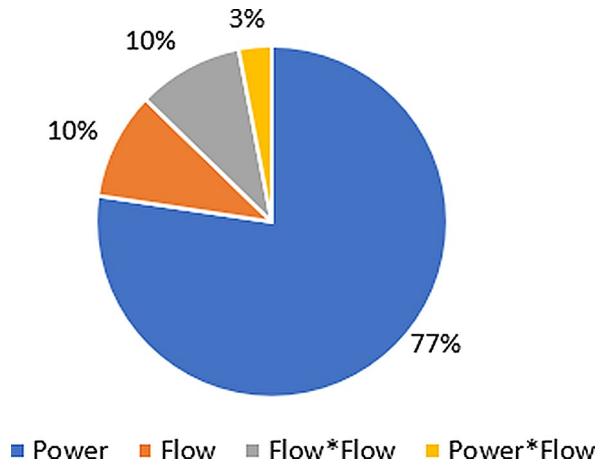


**Fig. 6** Contour plot for Ar 752 nm intensity example

plasma power with an influence of 77%. The flow has 20% total influence, with half of this effect due to the quadratic flow term. The cross interaction between gas flow and applied plasma power has a minor effect.

Figure 6 presents the levels of intensity as a contour map. It is useful to identify combinations of plasma power and gas flow that yield a desirable intensity, or generally any type of plasma chemistry outcome. It can be seen that the highest intensities are obtained at high plasma power. Also, the gas flow rate exhibits a quadratic influence on the intensity (see model A equation in Sect. 2.2.2). Additional contour plots can be found in Figure SI-7.

Based on the model equation, we have also built dynamic prediction profilers, where the controlled parameters can be easily changed, and the response function (the fitted intensity) is calculated accordingly. Animations of the dynamic predictions are demonstrated in Figures SI-8 and SI-9.

The fitted emission intensity is thereby verified in this example case by comparison between the experimental data and the model calculated values. The calculated predicted intensities agree well with the experimental results, as shown in Figure SI-10, and the deviations of the predicted values from the measured data were within approximately 4% (Table SI-4).

It should be noted that OES data can be utilized to deduce the relative density of excited species. Determination of the absolute density values requires more advanced calculations (as will be explained in the next section), whereas the relative density can be easily calculated as a ratio between the emission intensities. This method is described in several studies [124–126].

## Theoretical cold-plasma calculations– Model B

To continue the analysis and obtain insights into the plasma-chemistry reactions occurring in the plasma reactor, we will examine here the data extracted from the 1D theoretical model B, such as potential and the electric field, electron temperature and the densities of the various species, as a function of time and space, and compare to the experimental observations where possible. For an illustration of the pathways common in Ar plasma kinetics mechanisms, see for example Fig. 5 of Reference [127].

### Model B1

The results of the 1D model paint the following picture of the plasma dynamics. RF currents and voltages applied to the electrode create a sheath between the electrode and the bulk plasma and lead to collisionless heating in the sheath, and ohmic heating in the bulk [128]. In the case of RF power, the motion of the sheath is sinusoidal, and it must momentarily vanish during each cycle, signifying a moment at which the potential difference between the electrode and the plasma equals zero. This allows for the neutralization of the accumulated ion charge during that cycle [128]. The sheath thickness exhibits a sinusoidal pattern in time: while the sheath near  $x=0$  expands, during one half RF cycle, the sheath near  $x=10$  contracts, and vice versa. Figure 7 illustrates the electric field (a), and the potential (b) calculated from the model as a function of time and gap length.

It can be seen, as expected, that the center of the plasma gap (the bulk region) is the quasi-neutral region, where the potential and electric field are very low (compared to the sheaths), but not zero. This low electric field should sustain the plasma glow. The sinusoidal behavior and the sheaths' motion can be seen along the time axis near  $x=0$  and  $x=10$ .

The temperature profile over the gap length, that is characterized by high temperatures proximal to the electrodes and very moderate in the bulk, as expected in RF low-pressure plasma, has been demonstrated through the simulation.

Figure 8 shows the average electron temperature over an RF cycle as a function of power (a) and gas flow rate (b). In general, the temperature is very high in the sheath region, and much lower (a few eV) and fairly constant in the bulk area. At constant gas flow rate, the

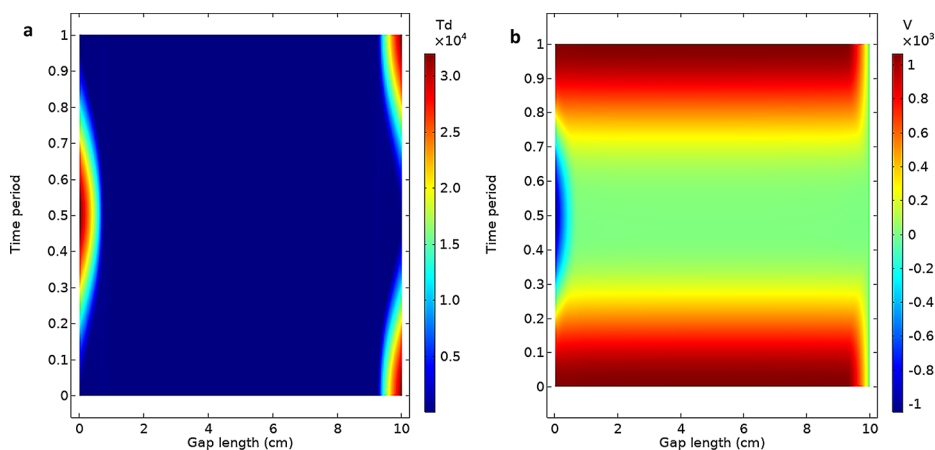


**Fig. 7** (a) Electric field and (b) potential along the plasma gap and a period of time for 100 W applied power and 50 sccm (225 mTorr)

electron temperature increases with increasing power. At constant applied power, the electron temperature decreases with increasing flow rate due to higher pressure and collision rate. This electron temperature behavior is with good agreement with the study presented in [129]. This behavior can be seen also in Figure SI-11, which shows a dynamic quantitative correlation between power, flow and electron temperature. The modeled temperature in this prediction profiler is the average over RF cycle and gap length. While the average temperature over the entire plasma gap depends on power, the average temperature over the bulk region remains constant when changing the power. This behavior is attributed to the sheath effect, which refers to the dynamic behavior of charged particles near the electrode surfaces. The sheath region is characterized by an intense electric field that accelerates charged particles, particularly electrons. Electrons gain kinetic energy from the electric field and exhibit higher energy levels, leading to an elevated electron temperature. This energy is then transferred to other species through collisions, increasing the overall energy of the particles in the sheath. The electrons are repelled by the electric field and therefore their density is depleted near the electrodes.

Pareto analysis indicates that the power contributes 50% of the effect on the average temperature over the entire plasma gap, the flow contributes 34% and the interaction between them 16%. These results agree nicely with the previously reported equivalent circuit model presented in [81]. Further details regarding the Pareto analysis are shown in Figure SI-12. Importantly, we show that a desirable temperature within the plasma can be tuned and controlled by simply setting the corresponding operation conditions obtained from the model. Such a capability allows us to advance rational design of chemical reactors from first principles, by offering the possibility of tailoring reactor conditions or chemical process behavior.

Accordingly, the simulation results for chemically relevant species are of especial interest. Figure 9 shows the electron density (a) and the densities of neutral and excited Ar (b). Figure 9(a) demonstrates an expected trend of increasing electron density as power is increased, for a given pressure. Such behavior may be explained by the increasing ionization rate, due to the increasing collision probability while increasing the power. The results are again in good agreement with previous theoretical studies using an equivalent circuit model

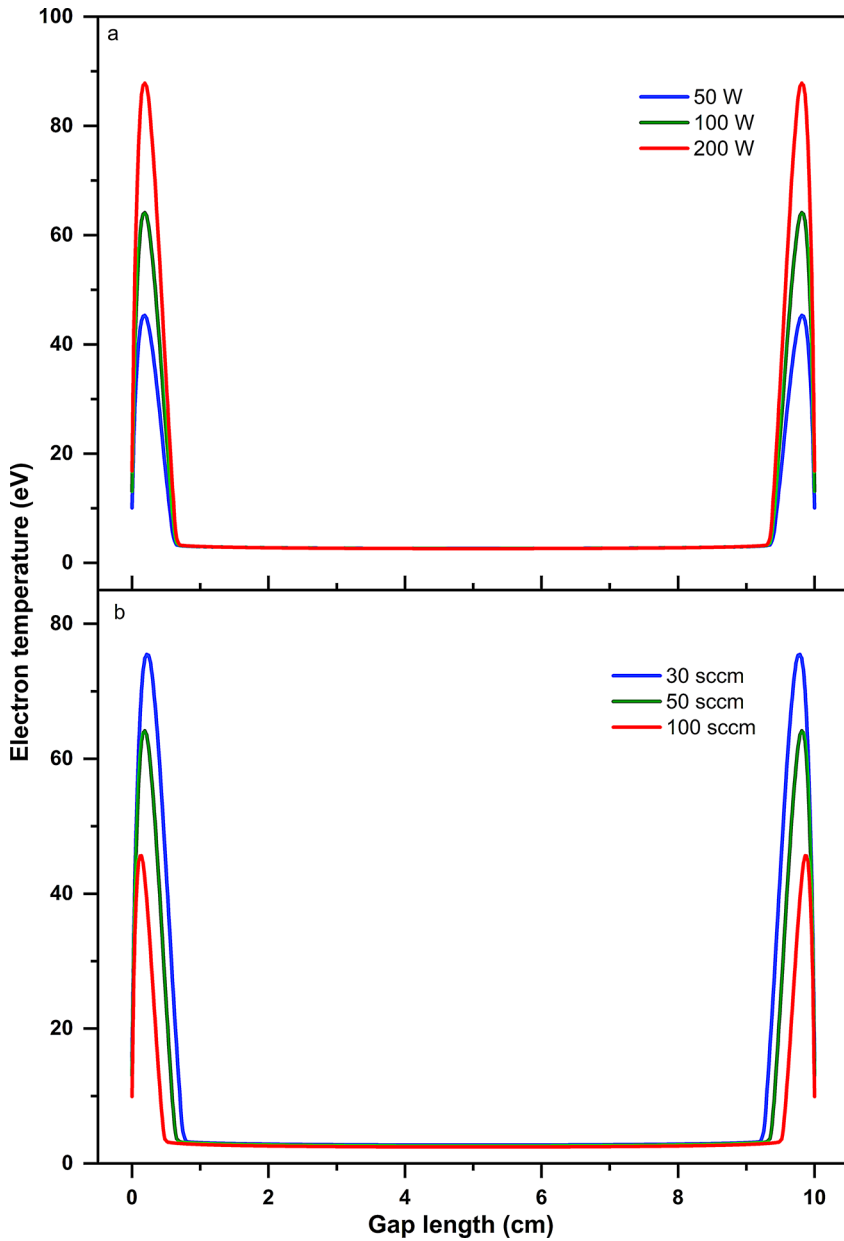


**Fig. 8** (a) Period-averaged electron temperature as function of plasma power, gas flow 50 sccm; (b) period-averaged electron temperature as function of gas flow, plasma power 100 W. The corresponding pressure for 30, 50 and 100 sccm is 158, 225 and 376 mTorr respectively

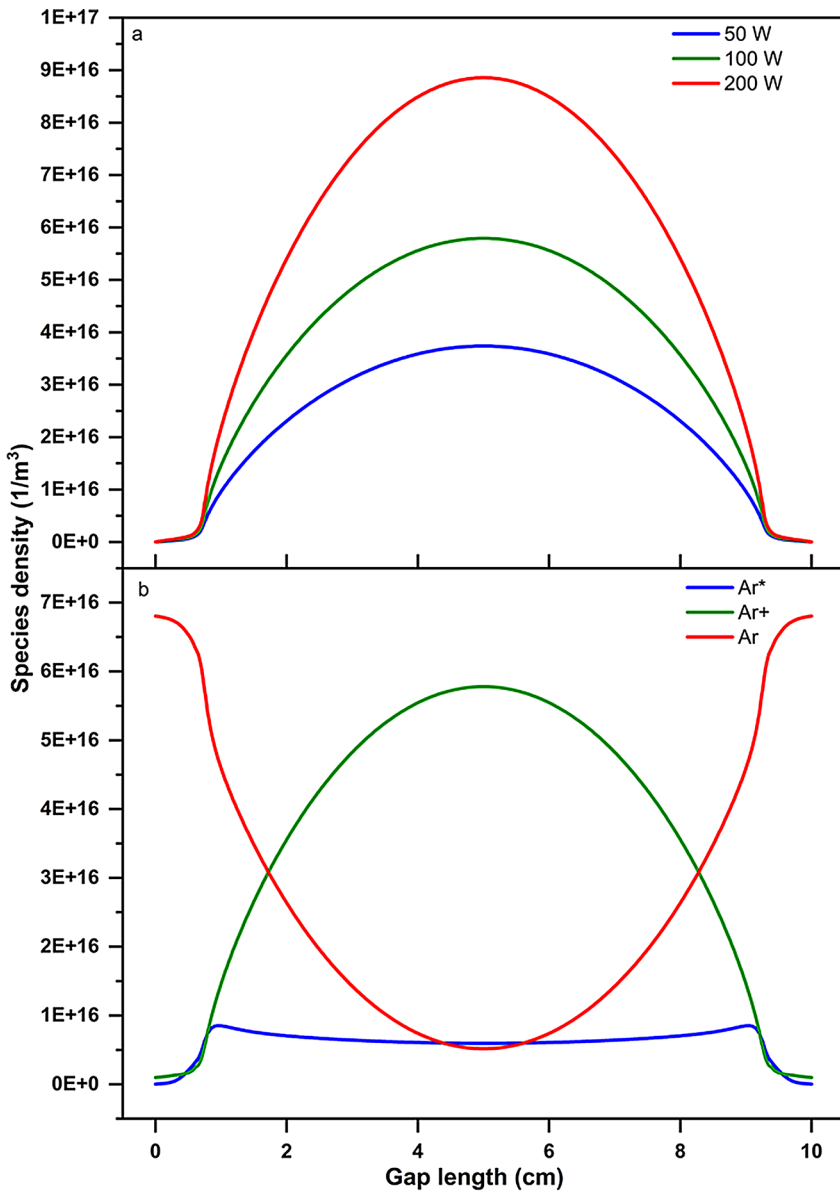


**Fig. 9** (a) Electron density at various applied powers and a constant flow rate of 50 sccm; (b) Ar, Ar\* and Ar<sup>+</sup> number density at 100 W and 50 sccm Ar, (Ar density is subtracted from 7.21E21 1/m<sup>3</sup> to allow sufficient range in its Y axis). The measured pressure for these conditions is 225 mTorr

[81]. The highest electron density is obtained in the center of the plasma, while near the wall the density is very low. This parabolic behavior can be attributed to the sheath dynamics in CCRF discharges. Models for such sheaths were presented by Lieberman [130], Godyak and Sternberg [131, 132], and more examples are presented in [133–136]. When positive ions collide with the electrodes, secondary electrons are emitted from the powered elec-

trode. However, these secondary electrons are quickly accelerated by the sheath electric field. Due to the high mobility of electrons, within an RF cycle they reach the electrode only momentarily, during sheath collapse. During the sheath expansion phase, electrons are pushed back from the electrodes to the center [137–139]. These electrons then ionize the background gas [140]. This periodic motion, combined with electron drift in the oscillating field, results in a time-averaged electron density that peaks in the center and decreases towards the electrodes, as seen in Fig. 9(a).

Figure 9(b) shows the expected opposite trends of ground state, excited state, and ion densities. The Ar ion density was compared to PIC-MC results, published by Becker et al., as their simulation was conducted under similar ranges of applied power and pressure to ours [104]. Becker et al. reported a maximum ion density of  $1.9\text{E}15\text{ 1/m}^3$ , calculated at 20 Pa, and a current density of  $10.1\text{ A/m}^2$ . Running our simulation under the exact same conditions yielded  $2.03\text{E}15\text{ 1/m}^3$ , which differs by merely 6.863% despite the different conditions, indicating that the values we obtain are entirely reasonable.

The reason we observe a minimum value for the argon density in the center is the increase in electron density at this point. The high-frequency electric field accelerates electrons, leading to increased electron energy. The electrons gain sufficient energy and mobility to collide with neutral argon atoms, causing ionization. This results in the production of positive ions and additional electrons. As a consequence, the electron density increases (and reaches a maximum at the center of discharge), leading to a decrease in the neutral argon density.

To validate our model, we examined the correlation between the measured intensity and the calculated density, as presented in Fig. 10. Theoretically, it can be seen that the relationship between density and intensity has the linear form of  $n=A*I+B$ , where B signifies the system's ignition threshold. The correlation is strong, with an R square of 0.96. It should be noted that the correlation between calculated density and emission intensity exists also with other (than 752 nm) measured wavelengths, such as 765, 802, 812 and 843 nm (with other correlation coefficients).

## Model B2

As mentioned above, model B2 is more comprehensive and takes into consideration a more detailed picture of transitions of Ar I from  $2p \rightarrow 1s$ . There are two metastable levels,  $1s5$  and  $1s3$  (in Paschen notation), with the excitation energies, 11.55 eV and 11.72 eV, respectively. These states are grouped together and called  $\text{Ar}^m$ . The other two  $1s$  levels are resonance states  $1s4$  and  $1s2$  with an excitation energy of 11.62 and 11.83 eV, respectively, are grouped together and called  $\text{Ar}^r$ . These levels are the source of vacuum ultraviolet (VUV) flux at 104.8 and 106.7 nm, which we cannot observe [138]. The ten  $4p$  levels, with energies between 12.91 and 13.48 eV [28, 89], are defined as state  $\text{Ar}^p$ . Figure 11 presents the density of the three excited states as a function of power. As expected, the density of the metastable level is highest and the density of  $4p$  state is lower. All densities increase with power.

Analyzing the power-dependent density lines shows that when the power changes from 20 to 250 W (the range where the plasma is most stable) the density of  $\text{Ar}^m$  varies by a factor of 2, while  $\text{Ar}^r$  and  $\text{Ar}^p$  exhibit variation of factor of 4.5 and 5 respectively. This suggests that the three states have different production and loss terms: the metastable state production and loss is mainly influenced by electron-driven processes, while the resonance and  $p$  state are

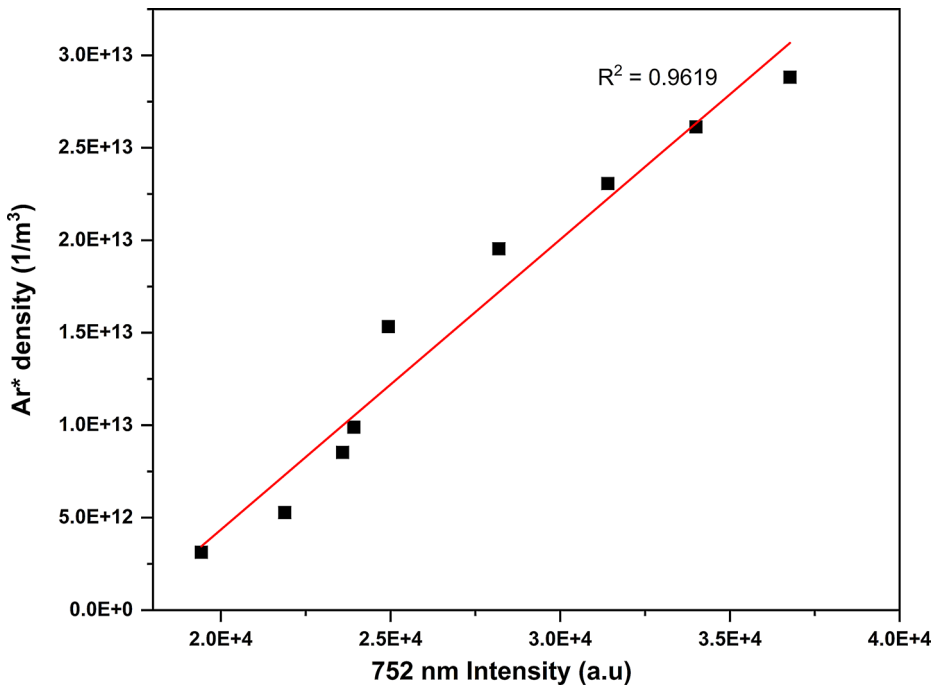


**Fig. 10** Calculated Ar\* density (period averaged) from the B1 model as a function of emission intensity at 752 nm. The intensities were measured in the range of 10–300 W and a constant gas flowrate of 50 sccm (225 mTorr)

produced by electron processes, but its depletion is attributed to radiation processes. These trends are in good agreement with other previous publications, for example in [138–140].

Figure 12 shows the density profile along the gap length for all the three excited states. The three profiles exhibit similar behavior: maximum density in the sheath region and minimum density at the center of the plasma gap. This behavior is attributed to the temperature profile.

Figure 13 presents the density of Ar<sup>r</sup> state at various gas flow and a constant applied power of 50 W. It can be seen that the density increases with flow (pressure). These results are in good agreement with the results from the recently published PIC/MCC simulation conducted by Wen et al. [141]. Additional insights extracted from the simulation include production and loss analyses. For example, the generation of Ar<sup>r</sup> is predominantly attributed to R6, contributing 80% to the production. R26 constitutes 18.5% contribution, whereas R10 and R17 are negligible. Regarding loss mechanisms, R23 contributes a substantial 95% to the overall loss, R11 contributes 2%, while contributions from R4, R12, R14, and R19 are negligible. These findings are calculated for gas flow of 50 sccm (225 mTorr) and applied power of 50 W, but they are consistent across various combinations of applied power and flow rates, with the percentages exhibiting a similar pattern. The above findings are consistent with what was described in Fig. 11– the resonance state is produced by electron processes, but its depletion is attributed to radiation– and in agreement with previous publications, for example in [141].

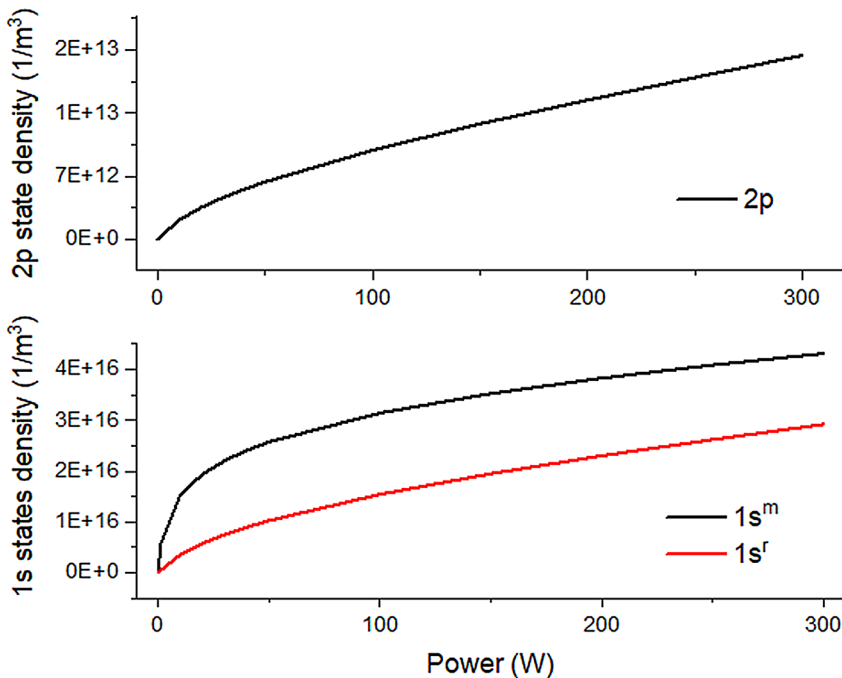


**Fig. 11** Excited state densities as function of applied power, at gas flow of 50 sccm (225 mTorr), calculated as an average over time period and gap length

It should be noted that both B1 and B2 models are accurate. The B2 model is more detailed than the B1 model, as it calculates three different excited states of argon, including metastable and resonance states, and aims to analyze their production and loss mechanisms. From a computational time perspective, the B1 model requires only a few minutes to converge, whereas the B2 model can take up to several tens of minutes, depending on the computer type. However, in both cases, the computation time is reasonable, so this difference is not a significant concern.

### Combining Model A and B: Post-Analysis

As discussed earlier, the intensity of any specific line, such as 752 nm, can be empirically modelled as a function of plasma power and gas flow rate. Any excited state density, calculated from model B2, can be described as a function of the measured emission intensities. Combining these two modeling approaches offers several benefits. First, it provides an efficient technique for quick estimation of species density as a function of controlled variables, enabling fast and practical insights into system behavior. Any desirable density of a specific excited state has a correlated emission intensity; the latter value has a combination of power and flow that are required to achieve this intensity. Second, by combining the strengths of non-invasive and easy to implement OES measurement with deeper theoretical understanding of plasma properties, such as electron temperature and species densities, we gain a holistic view of the plasma system, enabling the prediction and optimization of specific conditions for desired outcomes.

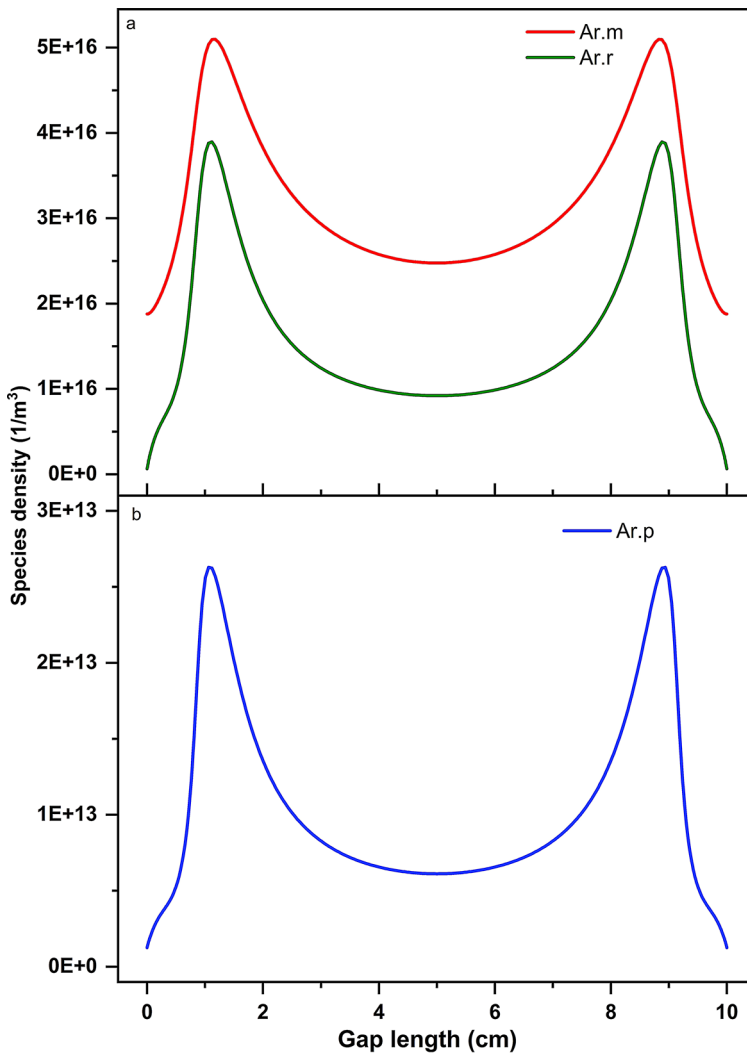


**Fig. 12** Excited state densities as function of gap length, at gas flow of 50 sccm (225 mTorr) and applied power of 100 W, calculated as an average over time period

This capability is demonstrated in Fig. 14, which shows the density of the  $\text{Ar}^{\text{P}}$  and  $\text{Ar}^{\text{r}}$  states as a function of the emission intensity at 752 nm. The figure demonstrates that the intensity of the 752 nm line exhibits a strong correlation with the density of the excited states. By measuring this intensity using OES, the density can be determined quickly, offering a faster alternative to the more complex process of calculating the density through simulations or models.

This integration is particularly significant because it allows for cross-validation between experimental measurements and theoretical predictions. By analyzing the relationship between measured metrics, such as emission intensity, and calculated plasma properties, such as species density, we gain confidence in both the experimental setup and the modeling

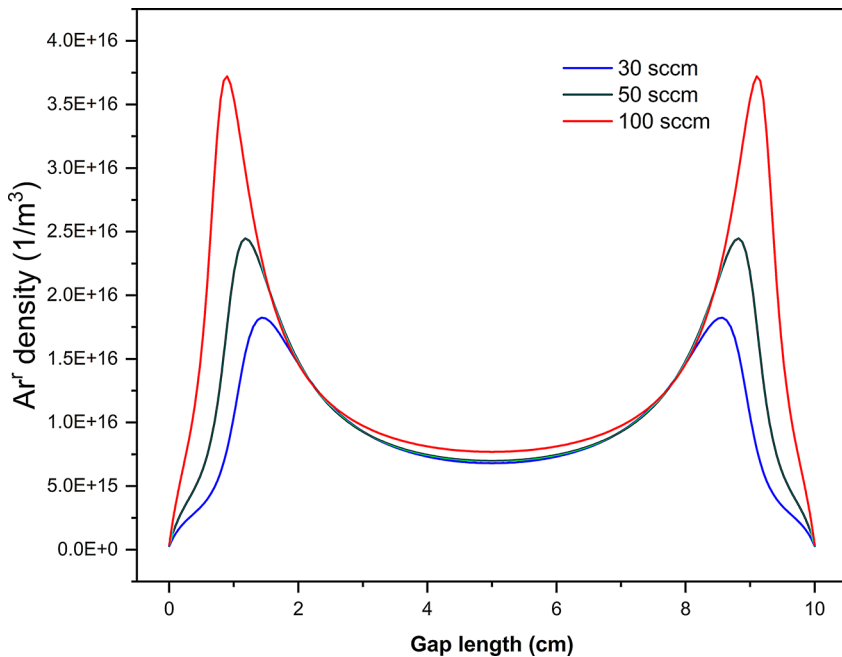


**Fig. 13** Ar<sup>+</sup> density as function of gap length at various gas flow and a constant applied power of 50 W, calculated as an average over time period

approach. A reasonable correlation between these metrics strengthens the reliability of the experimental results, confirming they were conducted effectively, while also validating the model.

## Conclusions and Future Work

In this study, we presented our strategy of modeling LPP of Argon alone using both multivariate analysis of measured data and theoretical simulations. The analysis of the main signals of argon under plasma conditions allowed us to understand how the peaks behave with the operational parameters (plasma power and gas flow rates). We have learned from the analysis present in this paper what is the contribution of each working condition on the desirable outcomes of the Ar LPP. Moreover, we clearly see how behavior of a characteristic peak tracks in good agreement with the intrinsic properties of the bulk plasma. Combining the multivariate method with theoretical models gives us a direct and fast estimation of densities of various species, temperatures, electric field, potential data, reaction rates and more.

The combination of statistical techniques with experimental data is particularly valuable in plasma science, where the complexity and nonlinearity of plasma behavior often present significant challenges. Statistical methods such as multivariate analysis enable the extraction of meaningful patterns from multidimensional datasets, highlighting critical parameters and their interactions that may otherwise remain obscured.

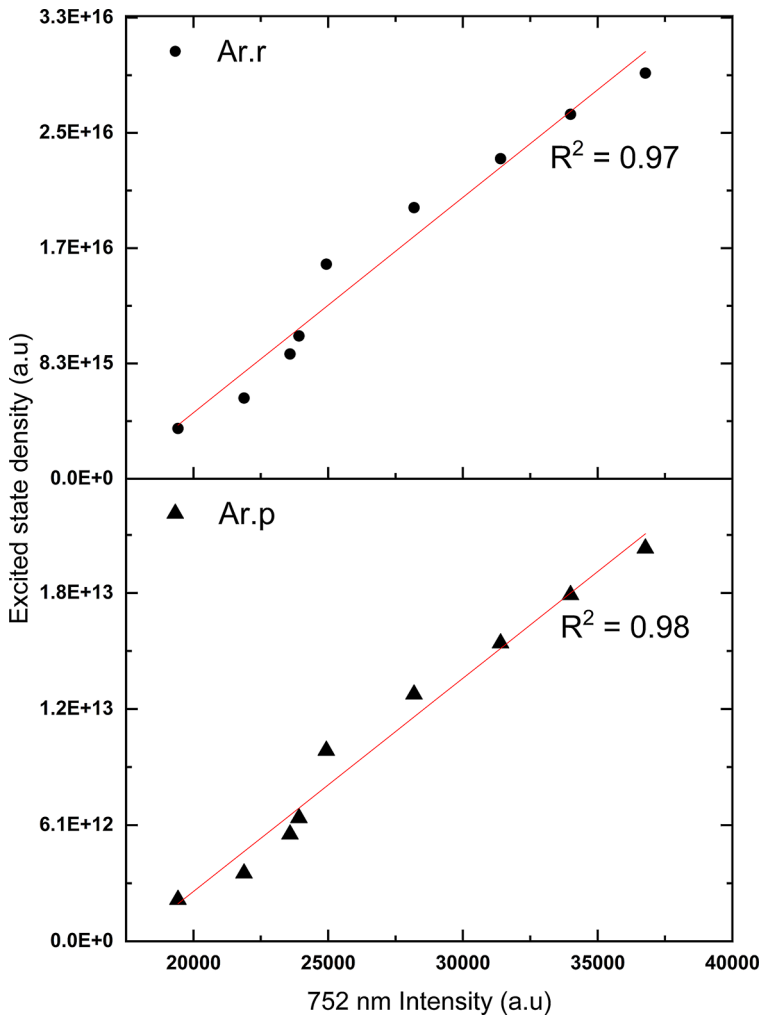


**Fig. 14** Excited state densities (calculated from model B2) as function of emission intensity measured at 752 nm, at gas flow of 50 sccm (225 mTorr). Densities are calculated as an average over time period and gap length

While our study focuses on relatively straightforward plasma chemistry, the applicability of this approach is much broader. We anticipate that a similar approach, when applied to more complex chemistry, has the potential to enhance our ability to understand plasma-chemical behavior and to predict chemical reaction mechanisms and plasma properties as well. This highlights the versatility and scalability of the proposed methodology in advancing plasma diagnostics and modeling.

It should be noted that analyzing more complex chemistry, such as plasma containing argon and water vapor, necessitates the inclusion of tens of additional reactions, including radiative reactions. Interpreting complex gas mixtures requires a detailed database that encompasses radiation reaction mechanisms. Without such a database, achieving a com-

prehensive understanding of the plasma behavior, including species generation and loss processes, may not be possible.

Subsequent work already in progress will build on the insights and knowledge presented here, focusing first on addition of nitrogen to the already studied set of Argon based plasma reactions. Detecting species such as hydrogen that are produced from water decomposition will be achieved by employing a higher resolution spectrometer. This next step will then allow us to continue to the even more complex plasma chemistry of organic molecular mixtures such as found in plastic waste, which as a practical matter typically are accompanied by water content. Our major goal for the future direction of this research is to better understand chemical reaction mechanisms related to waste decomposition applications.

**Supplementary Information** The online version contains supplementary material available at <https://doi.org/10.1007/s11090-025-10563-2>.

**Acknowledgements** This project has received funding from the Pazy foundation, Israel Atomic Energy Commission (IAEC) (Grant number 284-21), the Israeli Ministry of Energy (MoE) No. 3-18282/221-17-025 and the European Research Council (ERC) under the European Union’s Horizon 2020 research and innovation program (Grant Agreement 848668).

**Author Contributions** S.A., A.K., and J.H.B were the main contributors to the design and conception of the study. S.A and S.H.L. conducted experiments, with technical assistance from A.L., and analyzed the data. S.A. performed the modeling. I.R. contributed to project management. The manuscript was written by S.A, with assistance from H.Z. and J.H.B. All authors read and approved the final manuscript.

**Funding** Open access funding provided by Ben-Gurion University.

**Data Availability** No datasets were generated or analysed during the current study.

## Declarations

**Competing Interests** The authors declare no competing interests.

**Open Access** This article is licensed under a Creative Commons Attribution 4.0 International License, which permits use, sharing, adaptation, distribution and reproduction in any medium or format, as long as you give appropriate credit to the original author(s) and the source, provide a link to the Creative Commons licence, and indicate if changes were made. The images or other third party material in this article are included in the article’s Creative Commons licence, unless indicated otherwise in a credit line to the material. If material is not included in the article’s Creative Commons licence and your intended use is not permitted by statutory regulation or exceeds the permitted use, you will need to obtain permission directly from the copyright holder. To view a copy of this licence, visit <http://creativecommons.org/licenses/by/4.0/>.

## References

1. Meichsner J, Schmidt M, Schneider R, Wagner H-E (eds) (2013) *Nonthermal plasma chemistry and physics*. CRC, Boca Raton
2. Ruj B, Ghosh S (2014) Technological aspects for thermal plasma treatment of municipal solid waste - A review. *Fuel Process Technol* 126:298–308
3. Sikarwar VS, Hrabovský M, Van Oost G, Pohořelý M, Jeremiáš M (2020) Progress in waste utilization via thermal plasma. *Prog Energy Combust Sci* 81:100873
4. Huang H, Tang L (2007) Treatment of organic waste using thermal plasma pyrolysis technology. *Energy Convers Manag* 48:1331–1337
5. Sanito RC, You SJ, Wang YF (2021) Application of plasma technology for treating e-waste: A review. *J Environ Manage* 288

6. Ju Y (2015) Plasma assisted combustion: dynamics and chemistry. *Prog Energy Combust Sci* 48:21–83
7. Anuar Sharuddin SD, Abnisa F, Wan Daud WMA, Aroua MK (2016) A review on pyrolysis of plastic wastes. *Energy Conv Manag* 115:308–326
8. Punčochář M, Ruj B, Chatterjee PK (2012) Development of process for disposal of plastic waste using plasma pyrolysis technology and option for energy recovery. *Procedia Engineering, Elsevier Ltd*, pp 420–430
9. Rusu I (2007) Development trends of cold plasma reactors in the global context of carbon emission reduction. *Environ Eng Manag J* 6:211–217
10. Starikovskaia SM (2014) Plasma-assisted ignition and combustion: nanosecond discharges and development of kinetic mechanisms. *J Phys D* 47
11. Nehra V, Kumar A (2008) Atmospheric Non-Thermal plasma sources. *Int J Eng*; 53–68
12. Aubry O, Cormier JM (2009) Improvement of the diluted propane efficiency treatment using a non-thermal plasma. *Plasma Chem Plasma Process* 29:13–25
13. Ostrikov K, Cvelbar U, Murphy AB (2011) Plasma nanoscience: setting directions, tackling grand challenges. *J Phys D Appl Phys*; 44
14. Starikovskiy A, Aleksandrov N (2013) Plasma-assisted ignition and combustion. *Prog Energy Combust Sci* 39:61–110
15. Verreycken T, Bruggeman PJ (2014) OH density measurements in nanosecond pulsed discharges in atmospheric pressure N<sub>2</sub>-H<sub>2</sub>O mixtures. *Plasma Sources Sci Technol* 23:015009
16. Li L, Nikiforov A, Xiong Q et al (2013) OH radicals distribution in an Ar-H<sub>2</sub>O atmospheric plasma jet. *Phys Plasmas* 20:093502
17. Sarani A, Nikiforov AY, Leys C (2010) Atmospheric pressure plasma jet in ar and ar/H<sub>2</sub>O mixtures: optical emission spectroscopy and temperature measurements. *Phys Plasmas* 17:063504
18. Lazzaroni C, Lieberman MA, Lichtenberg AJ, Chabert P (2012) Comparison of a hybrid model to a global model of atmospheric pressure radio-frequency capacitive discharges. *J Phys D Appl Phys* 45:495204
19. Lazzaroni C, Chabert P, Lieberman MA, Lichtenberg AJ, Leblanc A (2012) Analytical numerical global model of atmospheric-pressure radio-frequency capacitive discharges. *Plasma Sources Sci Technol* 21:035013
20. Liu DX, Bruggeman P, Iza F, Rong MZ, Kong MG (2010) Global model of low-temperature atmospheric-pressure He+H<sub>2</sub>O plasmas. *Plasma Sources Sci Technol* 19:025018
21. Park G, Lee H, Kim G, Lee JK (2008) Global model of He/O<sub>2</sub> and Ar/O<sub>2</sub> atmospheric pressure glow discharges. *Plasma Processes Polym* 5:569–576
22. Park GY, Hong YJ, Lee HW, Sim JY, Lee JK (2010) A global model for the identification of the dominant reactions for atomic oxygen in He/O<sub>2</sub> atmospheric-pressure plasmas. *Plasma Processes Polym* 7:281–287
23. Reuter S, Von Woedtke T, Weltmann KD (2018) The kINPen - A review on physics and chemistry of the atmospheric pressure plasma jet and its applications. *J Phys D* 51:233001
24. Pappas D (2011) Status and potential of atmospheric plasma processing of materials. *J Vacuum Sci Technol A* 29:021301
25. Grill Alfred. *Cold plasma in materials fabrication: from fundamentals to applications*. Wiley-IEEE, (1994)
26. Stapelmann K, Fiebrandt M, Styrnoll T, Baldus S, Bibinov N, Awakowicz P (2015) Implications of electron heating and non-uniformities in a VHF-CCP for sterilization of medical instruments. *Plasma Sources Sci Technol* 24:034014
27. Steves S, Styrnoll T, Mitschker F, Bienholz S, Nikita B, Awakowicz P (2013) Characterization of low-pressure microwave and radio frequency discharges in oxygen applying optical emission spectroscopy and multipole resonance probe. *J Phys D Appl Phys* 46:445201
28. Palmero A, Van Hattum ED, Rudolph H, Habraken FHPM (2007) Characterization of a low-pressure argon plasma using optical emission spectroscopy and a global model. *J Appl Phys* 101:053306
29. Shul RJ, Pearton SJ (eds) (2000) *Handbook of advanced plasma processing techniques*. Springer, Berlin Heidelberg
30. Gomez S, Hoyos JH, Valdivia JA (2023) Particle-in-cell method for plasmas in the one-dimensional electrostatic limit. *Am J Phys* 91:225–234
31. Turner MM, Derzsi A, Donkó Z et al (2013) Simulation benchmarks for low-pressure plasmas: capacitive discharges. *Phys Plasmas*; 20
32. Takao Y, Matsuoka K, Eriguchi K, Ono K (2011) PIC-MCC simulations of capacitive RF discharges for plasma etching. 1051–1056
33. Sun A, Becker MM, Loffhagen D (2016) PIC/MCC simulation of capacitively coupled discharges: effect of particle management and integration. *Comput Phys Commun* 206:35–44

34. Wilczek S, Trieschmann J, Eremin D et al (2016) Kinetic interpretation of resonance phenomena in low pressure capacitively coupled radio frequency plasmas. *Phys Plasmas*; 23
35. Finelli F, Cerri SS, Califano F et al (2021) Bridging hybrid- and full-kinetic models with Landau-fluid electrons. *Astron Astrophys* 653:A156
36. Faraji F, Reza M, Knoll A (2022) Enhancing one-dimensional particle-in-cell simulations to self-consistently resolve instability-induced electron transport in hall thrusters. *J Appl Phys*; 131
37. Šimek J, Hrach R (2006) Comparison of collision treatment methods in PIC-MC plasma simulation. *Czech J Phys* 56:B1086–B1090
38. Ralchenko Y (ed) (2016) *Modern methods in Collisional-Radiative modeling of plasmas*. Springer International Publishing, Cham
39. Vinoth SP, Evans ES, Swanson CPS, Palmerduca E, Cohen SA (2022) Evaluation of a collisional radiative model for electron temperature determination in hydrogen plasma. *Rev Sci Instrum*; 93
40. Fox-Widdows E, Bowden MD, Hoshino K, Hatayama A, Osawa R, Tsubotani Y (2023) The development of a zero-dimensional collisional-radiative model for interpreting plasma emission in low temperature divertor plasmas in Tokamaks. *Front Phys*; 11
41. Mankelevich YA, Ashfold MNR, Ma J (2008) Plasma-chemical processes in microwave plasma-enhanced chemical vapor deposition reactors operating with C/H/Ar gas mixtures. *J Appl Phys* 104:113304
42. Tachibana K, Nishida M, Harima H, Urano Y (1984) Diagnostics and modelling of a methane plasma used in the chemical vapor deposition of amorphous carbon films. *J Phys D Appl Phys* 17:1727–1742
43. Sezer AO, Brand JI (2001) Chemical vapor deposition of Boron carbide. *Mater Sci Engineering: B* 79:191–202
44. Armaou A, Christofides PD (1999) Plasma enhanced chemical vapor deposition: modeling and control. *Chem Eng Sci* 54:3305–3314
45. Kushner MJ (1988) A model for the discharge kinetics and plasma chemistry during plasma enhanced chemical vapor deposition of amorphous silicon. *J Appl Phys* 63:2532–2551
46. Guo W, Sawin HH (2009) Review of profile and roughening simulation in microelectronics plasma etching. *J Phys D Appl Phys* 42:194014
47. Chang JP, Mahorowala AP, Sawin HH. Plasma-surface kinetics and feature profile evolution in chlorine etching of polysilicon. *Journal of Vacuum ScienceTechnology, Vacuum A* (1998) *Surfaces, and Films*; 16: 217–224
48. Anderson HM, Merson JA, Light RW (1986) A kinetic model for plasma etching silicon in a SF<sub>6</sub>/O<sub>2</sub> RF discharge. *IEEE Trans Plasma Sci* 14:156–164
49. Economou DJ (2017) Hybrid simulation of low temperature plasmas: A brief tutorial. *Plasma Processes Polym*; 14
50. Yadav HNS, Kumar M, Kumar A, Das M (2021) COMSOL simulation of microwave plasma Polishing on different surfaces. *Mater Today Proc* 45:4803–4809
51. Baldry M, Haidar LL, Akhavan B, Bilek MMM (2021) Continuum modelling of an asymmetric CCRF argon plasma reactor: influence of higher excited States and sensitivity to model parameters. *Plasma Processes Polym*; 18
52. Rebiai S, Bahouh H, Sahli S (2013) 2-D simulation of dual frequency capacitively coupled helium plasma, using COMSOL multiphysics. *IEEE Trans Dielectr Electr Insul* 20:1616–1624
53. Cheng J, Ji L, Wang K, Han C, Shi Y (2013) Two-dimensional simulation of inductively coupled plasma based on COMSOL and comparison with experimental data. *J Semicond* 34:066004
54. Brezmes AO, Breikopf C (2015) Fast and reliable simulations of argon inductively coupled plasma using COMSOL. *Vacuum* 116:65–72
55. Jia C, Linhong J, Yu Z, Yixiang S (2010) Fluid model of inductively coupled plasma etcher based on COMSOL. *J Semicond* 31:032004
56. Sohbatzadeh F, Soltani H (2018) Time-dependent one-dimensional simulation of atmospheric dielectric barrier discharge in N<sub>2</sub>/O<sub>2</sub>/H<sub>2</sub>O using COMSOL multiphysics. *J Theoretical Appl Phys* 12:53–63
57. Kortshagen U (1999) Heil. kinetic Two-Dimensional modeling of inductively coupled plasmas based on a hybrid kinetic approach. *IEEE Trans Plasma Sci* 27:1297–1309
58. Jayaraman B, Shyy W (2008) Modeling of dielectric barrier discharge-induced fluid dynamics and heat transfer. *Prog Aerosp Sci* 44:139–191
59. Schutz AE, Greenwood AD, Cartwright KL, Mardahl PJ (2004) Hybrid particle-fluid modeling of plasmas. The 31st IEEE International Conference on Plasma Science, 2004. ICOPS 2004. IEEE Conference, IEEE. 336–336
60. Lin Z, Chen L (2001) A fluid–kinetic hybrid electron model for electromagnetic simulations. *Phys Plasmas* 8:1447–1450
61. Hwang SW, Lee H-J, Lee HJ (2014) Effect of electron Monte Carlo collisions on a hybrid simulation of a low-pressure capacitively coupled plasma. *Plasma Sources Sci Technol* 23:065040

62. van Dijk J, Kroesen GMW, Bogaerts A (2009) Plasma modelling and numerical simulation. *J Phys D Appl Phys* 42:190301
63. Abramovic I, Alves EP, Greenwald M (2022) Data-driven model discovery for plasma turbulence modelling. *J Plasma Phys* 88:895880604
64. Samuell CM, Mclean AG, Johnson CA, Glass F, Jaervinen AE (2021) Measuring the electron temperature and identifying plasma detachment using machine learning and spectroscopy. *Rev Sci Instrum*; 92
65. Spinosa AG, Buscarino A, Fortuna L, Iafrati M, Mazzitelli G (2021) Data-driven order reduction in Hammerstein–Wiener models of plasma dynamics. *Eng Appl Artif Intell* 100:104180
66. Alves EP, Fiuza F (2022) Data-driven discovery of reduced plasma physics models from fully kinetic simulations. *Phys Rev Res* 4:033192
67. Takagi Y, Iwata N, d’Humieres E, Sentoku Y (2021) Multivariate scaling of maximum proton energy in intense laser driven ion acceleration. *Phys Rev Res* 3:043140
68. Djordjević BZ, Kemp AJ, Kim J et al (2021) Modeling laser-driven ion acceleration with deep learning. *Phys Plasmas*; 28
69. Park S, Seong J, Park Y et al (2024) Data-driven plasma science based plasma etching process design in OLED mass production referring to PI-VM. *Plasma Phys Control Fusion* 66:025014
70. Daly GA, Fieldsend JE, Hassall G, Tabor GR (2023) Data-driven plasma modelling: surrogate collisional radiative models of fluorocarbon plasmas from deep generative autoencoders. *Mach Learn Sci Technol* 4:035035
71. Hatfield PW, Gaffney JA, Anderson GJ et al (2021) The data-driven future of high-energy-density physics. *Nature* 593:351–361
72. O’Connor N, Milosavljević V, Daniels S (2011) Development of a real time monitor and multivariate method for long term diagnostics of atmospheric pressure dielectric barrier discharges: application to he, He/N<sub>2</sub>, and He/O<sub>2</sub> discharges. *Rev Sci Instrum*; 82
73. Gidon D, Pei X, Bonzanini AD, Graves DB, Mesbah A (2019) Machine learning for Real-Time diagnostics of cold atmospheric plasma sources. *IEEE Trans Radiat Plasma Med Sci* 3:597–605
74. Azari AR, Lockhart JW, Liemohn MW, Jia X (2020) Incorporating physical knowledge into machine learning for planetary space physics. *Front Astronomy Space Sci*; 7
75. Anirudh R, Archibald R, Asif MS et al (2023) 2022 Review of Data-Driven plasma science. *IEEE Trans Plasma Sci* 51:1750–1838
76. Marques L, Jolly J, Alves LL (2007) Capacitively coupled radio-frequency hydrogen discharges: the role of kinetics. *J Appl Phys* 102:063305
77. Cui R, Han R, Yang K et al (2020) Diagnosis of Helicon plasma by local OES. *Plasma Sources Sci Technol* 29:015018
78. Godyak VA, Piejak RB (1990) Abnormally low electron energy and heating-mode transition in a low-pressure argon RF discharge at 13.56 mhz. *Phys Rev Lett* 65:996–999
79. Reuter S, Winter J, Iseni S et al (2012) Detection of Ozone in a mhz argon plasma bullet jet. *Plasma Sources Sci Technol* 21:034015
80. Godyak VA, Piejak RB, Alexandrovich BM (2002) Electron energy distribution function measurements and plasma parameters in inductively coupled argon plasma. *Plasma Sources Sci Technol* 11:525–543
81. He X, Liu C, Zhang Y et al (2018) Diagnostic of capacitively coupled radio frequency plasma from electrical discharge characteristics: comparison with optical emission spectroscopy and fluid model simulation. *Plasma Sci Technol* 20:024005
82. Zhang Y, He X, Chen J et al (2014) Experimental and numerical investigations on microwave absorption by the cold collisional capacity-coupled-plasma. *IEEE Trans Plasma Sci* 42:2253–2258
83. Tu X, Chéron BG, Yan JH, Cen KF (2007) Electrical and spectroscopic diagnostic of an atmospheric double Arc argon plasma jet. *Plasma Sources Sci Technol* 16:803–812
84. Siepa S, Danko S, Tsankov TV, Mussenbrock T, Czarnetzki U (2014) On the OES line-ratio technique in argon and argon-containing plasmas. *J Phys D Appl Phys* 47:445201
85. Akatsuka H (2019) Optical emission spectroscopic (OES) analysis for diagnostics of electron density and temperature in non-equilibrium argon plasma based on collisional-radiative model. *Adv Physics: X* 4:257–281
86. Bogaerts A, Gijbels R, Vlcek J (1998) Collisional-radiative model for an argon glow discharge. *J Appl Phys* 84:121–136
87. Chung HK, Song MY, Kwon JW et al (2021) Population kinetics modeling of low-temperature argon plasma. *Atoms*; 9
88. Balcon N, Hagelaar GJM, Boeuf JP (2008) Numerical model of an argon atmospheric pressure RF discharge. *IEEE Trans Plasma Sci* 36:2782–2787
89. Nikolić M, Newton J, Sukenik CI, Vušković L, Popović S (2015) Measurements of population densities of metastable and resonant levels of argon using laser induced fluorescence. *J Appl Phys* 117:023304

90. Gaens W, Van, Bogaerts A (2013) Kinetic modelling for an atmospheric pressure argon plasma jet in humid air. *J Phys D Appl Phys* 46:275201
91. <https://www.jmp.com>
92. <https://www.comsol.com/plasma-module>
93. [https://doc.comsol.com/6.3/docserver/#!/com.comsol.help.plasma/plasma\\_ug\\_plasma.09.41.html](https://doc.comsol.com/6.3/docserver/#!/com.comsol.help.plasma/plasma_ug_plasma.09.41.html)
94. Teunissen J (2020) Improvements for drift-diffusion plasma fluid models with explicit time integration. *Plasma Sources Sci Technol* 29:015010
95. Datta S, Han JG, Kumar R, Sahu BB (2024) Experimental studies and COMSOL 1-D simulation in ar capacitively coupled plasmas. *AIP Adv*; 14
96. Yang J, Wu A, Li X et al (2017) Experimental and simulation investigation of electrical and plasma parameters in a low pressure inductively coupled argon plasma. *Plasma Sci Technol* 19:115402
97. Ochoa Brezmes A, Breitkopf C (2014) Simulation of inductively coupled plasma with applied bias voltage using COMSOL. *Vacuum* 109:52–60
98. Gao F, Zhang Y-R, Li H, Liu Y, Wang Y-N (2017) Spatial distributions of plasma parameters in inductively coupled hydrogen discharges with an expansion region. *Phys Plasmas*; 24
99. Zhou C, Rafatov I, Wang Y et al (2024) On fundamental inconsistencies in a commonly used modification of a fluid model for glow discharge. *Plasma Sources Sci Technol* 33:077001
100. Sigenefer F, Ellis J, Harhausen J, Lang N, van Helden JH (2022) Verified modeling of a low pressure hydrogen plasma generated by electron cyclotron resonance. *Plasma Sources Sci Technol* 31:105011
101. Becker MM, Kählerlert H, Sun A, Bonitz M, Loffhagen D (2017) Advanced fluid modeling and PIC/MCC simulations of low-pressure CCRF discharges. *Plasma Sources Sci Technol* 26:044001
102. Eremin D, Hemke T, Mussenbrock T (2016) A new hybrid scheme for simulations of highly collisional RF-driven plasmas. *Plasma Sources Sci Technol* 25:015009
103. Derzsi A, Hartmann P, Korolov I, Karácsony J, Bánó G, Donkó Z (2009) On the accuracy and limitations of fluid models of the cathode region of Dc glow discharges. *J Phys D Appl Phys* 42:225204
104. Kang W, Hur M, Song Y, Hong S (2013) Numerical simulation of atmospheric-pressure non-equilibrium plasmas: status and prospects. *Internat J Plasma Environ Sci Technol* 7:104–108
105. Popoli A, Ragazzi F, Pierotti G, Neretti G, Cristofolini A (2023) A Boltzmann electron drift diffusion model for atmospheric pressure Non-Thermal plasma simulations. *Plasma* 6:393–407
106. Grubert GK, Becker MM, Loffhagen D (2009) Why the local-mean-energy approximation should be used in hydrodynamic plasma descriptions instead of the local-field approximation. *Phys Rev E* 80:036405
107. Donkó Z, Hartmann P, Kutasi K (2006) On the reliability of low-pressure Dc glow discharge modelling. *Plasma Sources Sci Technol* 15:178–186
108. Pancheshnyi S, Biagi S, Bordage MC et al (2012) The LXCat project: electron scattering cross sections and swarm parameters for low temperature plasma modeling. *Chem Phys* 398:148–153
109. Pitchford LC, Alves LL, Bartschat K et al (2013) Comparisons of sets of electron-neutral scattering cross sections and swarm parameters in noble gases: I. Argon. *J Phys D Appl Phys* 46:334001
110. Carbone E, Graef W, Hagelaar G et al (2021) Data needs for modeling low-temperature non-equilibrium plasmas: the LXCat project, history, perspectives and a tutorial. *Atoms* 9:1–41
111. Pitchford LC, Alves LL, Bartschat K et al (2017) LXCat: an Open-Access, Web-Based platform for data needed for modeling low temperature plasmas. *Plasma Processes Polym* 14:1600098
112. Bartschat K (2013) Computational methods for electron-atom collisions in plasma applications. *J Phys D Appl Phys* 46:334004
113. Tennyson J, Rahimi S, Hill C et al (2017) A new database of plasma chemistries and reactions. *Plasma Sources Sci Technol QDB*:26: 055014
114. Phelps AV (2023) Phelps database, [www.lxcat.net](http://www.lxcat.net), retrieved
115. S.F. Biagi. [www.lxcat.net/Biagi](http://www.lxcat.net/Biagi). (2011). <https://physics.nist.gov>
116. Hjartarson AT, Thorsteinsson EG, Gudmundsson JT (2010) Low pressure hydrogen discharges diluted with argon explored using a global model. *Plasma Sources Sci Technol* 19:065008
117. Park SH (1996) Robust design and analysis for quality engineering. Springer, New York, NY
118. Petchrompo S, Coit DW, Brintrup A, Wannakrairot A, Parlikad AK (2022) A review of Pareto pruning methods for multi-objective optimization. *Comput Ind Eng* 167:108022
119. Chapman JL, Lu L, Anderson-Cook CM (2014) Process optimization for multiple responses utilizing the Pareto front approach. *Qual Eng* 26:253–268
120. Bakowski B, Hancock G, Peverall R, Prince SE, Ritchie GAD, Thornton LJ (2005) Diode laser measurements of the ar 3p54s1 excited States in an inductively coupled RF plasma. *J Phys D Appl Phys* 38:2769–2777
121. Hebner GA (1996) Spatially resolved, excited state densities and neutral and ion temperatures in inductively coupled argon plasmas. *J Appl Phys* 80:2624–2636

122. Leonhardt D, Eddy CR, Shamamian VA, Fernsler RF, Butler JE (1998) Argon metastables in a high density processing plasma. *J Appl Phys* 83:2971–2979
123. Lee H-C, Chung C-W (2015) Effect of electron energy distribution on the hysteresis of plasma discharge: theory, experiment and modeling. *Sci Rep* 5:15254
124. Chabert P, Braithwaite N (2011) *Physics of Radio-Frequency plasmas*. Cambridge University Press
125. Samir T, Liu Y, Zhao L (2018) Study on effect of neutral gas pressure on plasma characteristics in capacitive RF argon glow discharges at low pressure by fluid modeling. *IEEE Trans Plasma Sci* 46:1738–1746
126. Lieberman MA (1989) Dynamics of a collisional, capacitive RF sheath. *IEEE Trans Plasma Sci* 17:338–341
127. Godyak VA, Sternberg N (1990) Dynamic model of the electrode sheaths in symmetrically driven RF discharges. *Phys Rev (Coll Park)* 42:2299–2312
128. Sternberg N, Godyak V (2007) The Bohm Plasma-Sheath model and the Bohm criterion revisited. *IEEE Trans Plasma Sci* 35:1341–1349
129. Panagopoulos T, Economou DJ (1999) Plasma sheath model and ion energy distribution for all radio frequencies. *J Appl Phys* 85:3435–3443
130. Miller PA, Riley ME (1997) Dynamics of collisionless Rf plasma sheaths. *J Appl Phys* 82:3689–3709
131. Kawamura E, Vahedi V, Lieberman MA, Birdsall CK (1999) Ion energy distributions in RF sheaths; review, analysis and simulation. *Plasma Sources Sci Technol* 8:R45–R64
132. Bose D, Govindan TR, Meyyappan M (2000) Ion dynamics model for collisionless radio frequency sheaths. *J Appl Phys* 87:7176–7184
133. Hemke T, Eremin D, Mussenbrock T et al (2012) Ionization by bulk heating of electrons in capacitive radio frequency atmospheric pressure microplasmas. *Plasma Sources Sci Technol* 22:015012
134. Dittmann K, Matyash K, Nemschokmichal S, Meichsner J, Schneider R (2010) Excitation mechanisms and sheath dynamics in capacitively coupled Radio-Frequency oxygen plasmas. *Contrib Plasma Phys* 50:942–953
135. Rauf S, Bera K, Collins K (2010) Power dynamics in a low pressure capacitively coupled plasma discharge. *Plasma Sources Sci Technol* 19:015014
136. Wilczek S, Schulze J, Brinkmann RP, Donkó Z, Trieschmann J, Mussenbrock T (2020) Electron dynamics in low pressure capacitively coupled radio frequency discharges. *J Appl Phys* 127:181101
137. Kovalev AS, Kurchikov KA, Proshina OV, Rakhimova TV, Vasilieva AN, Voloshin DG (2019) Determination of the excited argon States densities in high-frequency capacitive discharge. *Phys Plasmas* 26:123501
138. Malyshev M, Donnelly V (1999) Trace rare gases optical emission spectroscopy: nonintrusive method for measuring electron temperatures in low-pressure, low-temperature plasmas. *Phys Rev E* 60:6016–6029
139. Vasilieva AN, Voloshin DG, Kovalev AS, Kurchikov KA (2015) Measurements of the populations of metastable and resonance levels in the plasma of an RF capacitive discharge in argon. *Plasma Phys Rep* 41:426–433
140. Wen D-Q, Krek J, Gudmundsson JT et al (2023) On the importance of excited state species in low pressure capacitively coupled plasma argon discharges. *Plasma Sources Sci Technol* 32:064001

**Publisher's Note** Springer Nature remains neutral with regard to jurisdictional claims in published maps and institutional affiliations.